Chapter 13

Forward scatter radar

Marina Gashinova[1], Liam Daniel[1], Alexander Myakinkov[2] and Mikhail Cherniakov[1]

Abstract

Forward scatter radar (FSR) is historically thought of as the first type of bistatic radar. Research on FSR has been predominantly focussed on its ability to serve as an electronic fence, and it has already proven the FSR's excellent detection and target motion parameter estimation capabilities. Recently, a wave of interest has emerged in FSR; first, this is a consequence of the introduction of 'stealth' targets. These targets have a significantly reduced radar cross-section (RCS) because of their specific shapes and/or coatings which may greatly suppress backscattering, yet their shadows will still render them perfectly 'visible' to FSR. Second, interest in FSR has appeared because of the establishment of passive coherent location concepts where illuminators of opportunity are used to form a bistatic radar network.

This chapter provides an overview of FSR, theory and phenomenology and further discusses its capabilities and limitations.

13.1 Introduction

Forward scatter radar (FSR) is historically thought of as the first type of bistatic radar. There is however a fundamental difference; while FSR could be viewed as subclass of bistatic radar where the bistatic angle is close to 180°, the physical operational principle is essentially different from that of bistatic radar. In FSR the target signature is formed as a result of interference between the direct path (or leakage) signal and the scattered signal from the target, called shadow radiation. While the target is in motion the scattering mechanism undergoes a fundamental change—bistatic scattering (mainly of the reflective nature) when the receiver is outside the target main shadow lobe which transforms into purely shadow radiation at the time when the target crosses the baseline casting shadow upon the receiver.

[1] Department of Electronic Electrical and Systems Engineering, The University of Birmingham, UK
[2] Nizhny Novgorod State Technical University, Russia

Because of such a mechanism, the research on FSR has predominantly focused on its ability to serve as an electronic fence and FSR's excellent detection and target motion parameter estimation capabilities have already been proven.

Recently a wave of interest has emerged in FSR. Firstly, this is a consequence of the introduction of 'stealth' targets. These targets have a significantly reduced radar cross-section (RCS) because of their specific shapes and/or coatings which may greatly suppress backscattering; yet their shadows will still render them visible to FSR. Secondly, interest in FSR has appeared because of the establishment of passive coherent location (PCL) concept where illuminators of opportunity are used to form a bistatic radar network.

In this chapter, we initially discuss the topology of FSR in relation to mono and bistatic radar, look at the phenomenology of FSR and explain the forward scatter radar cross section and forward scatter effect as a manifestation of shadow radiation. The target signature model is then described in Section 13.3 in fundamental terms of a phase signature modulated by the forward scatter cross section (FSCS) envelope. Power budget analysis for target detection and optimal signal processing for target motion parameter estimation are presented and the performance of experimental FSR systems is demonstrated with experimental results in diverse ground and maritime scenarios. Section 13.4 is dedicated to the analysis and characterisation of FSR clutter and Section 13.5 closes the chain of application domains by giving the principles for airborne target detection and tracking, supported by experimental results.

13.2 Radar topology and electromagnetic wave scattering mechanism

13.2.1 Monostatic, bistatic and forward scatter radar topology

The two main radar types as classified by their configurations are monostatic radar which comprise the majority of modern radars and bistatic radar which are currently the subject of intensive study. In monostatic radar, depicted in Figure 13.1(a), both transmit (Tx) and receive (Rx) antennas are co-located and point towards a region to observe a target (Tg) at a range R_{ms}. In bistatic radar, Figure 13.1(b), the distance between Tx and Rx antennas, d, referred also as the baseline, is comparable with the ranges of the target to the transmitter, R_{t} and to the receiver R_{r}. Three points, Tx, target and Rx, form a bistatic triangle which lie in a bistatic plane.

There are three relevant angles in this plane, θ_{t} and θ_{r}, which are the transmitter and the receiver look angles and $\beta = 180 - (\theta_{\mathrm{t}} + \theta_{\mathrm{r}})$ is the bistatic angle. Within the bistatic radar configurations, there is a special case, where $R_t + R_r \approx d$ and consequently $\beta \approx 180°$, which is known as FSR and is shown in Figure 13.1(c), this subclass of bistatic radar is the focus of this book chapter. Such radars are also known in the literature as line radar, electronic fences and flutter radar [1,2], the historical development and state of the art descriptions can be found in such texts as [1,3]. The forward scatter (FS) topology lends itself towards systems where

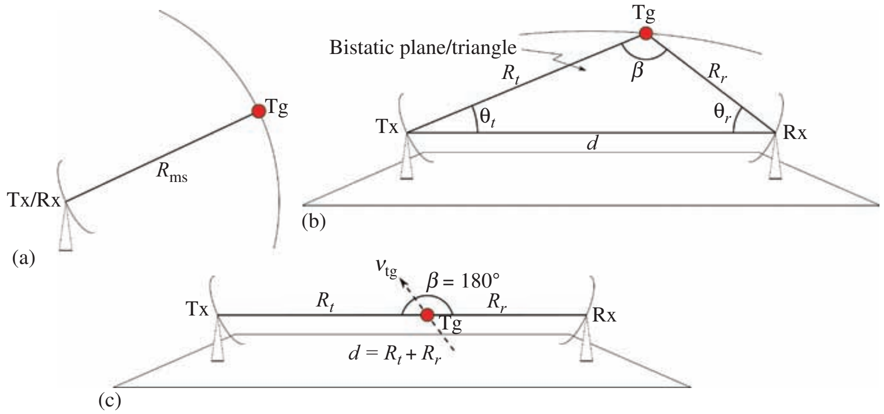

Figure 13.1 Overview of radar topologies. (a) Monostatic radar, (b) bistatic radar and (c) forward scatter radar shown with a target (Tg) crossing the baseline

antennas face each other (when considering directional antennas) and target detection occurs in spatial regions on or very close to the baseline. It is immediately obvious that there is no range resolution in such a radar system – irrelevant of the position of the targets along the baseline, all scattered signals as well as the direct path signal (DPS) from the transmitter reach the receiver at the same time. This observation also follows from the known equation for bistatic radar range resolution, $\Delta R_{\mathrm{bs}}^{\psi}$, which is measured along the bi-sector of the bistatic angle and calculated as follows [1 (p.131)]:

$$\Delta R_{\mathrm{bs}}^{\psi} \approx \frac{\Delta R_{\mathrm{bs}}}{\cos\psi} = \frac{c}{2\Delta F \cos(\beta/2)\cos\psi} \tag{13.1}$$

where ψ is the second target's angular deviation from the bistatic bisector of the first target and ΔF is the ranging signal bandwidth. From (13.1), it follows that as $\beta \to 180°$, $\Delta R_{\mathrm{bs}}^{\psi} \to \infty$, i.e. the range resolution is dramatically reduced and only wide or ultra-wideband signals introduce some range resolution [4,5]. This obvious drawback of FSR nevertheless gives rise to the reception of non-fluctuating target signals even when scattered from highly manoeuvrable targets. As a result, the maximum coherent analysis time in FSR is equal to the target visibility time T_v. Thus, an absence of range resolution in FSR is partly compensated by enhanced frequency (Doppler) resolution [6,7] which is considered in Section 13.2.2.1.

In FSR, the dominating physical principle of target observation is the forward scattering of electromagnetic (EM) waves (also known in optics as shadowing), as opposed to 'backscattering' in monostatic radar and bistatic radar, where in the absence of a target, the transmitted signal does not arrive at the receiver input unless there is a parasitic leakage signal (LS) present. In contrast, in FSR, the transmitted signal is fundamentally acquired by the receiver, the DPS then serves as a carrier for modulation caused by scattering/shadowing from the target in the forward direction when in the vicinity of the baseline. Target detection and motion parameter estimation is therefore based on DPS perturbations as opposed to received energy increase as in monostatic radar and bistatic radar. Thus in FSR, the DPS presence is a necessary pre-requisite. Such signals can be acquired by different technical ways: direct and scattered signal self-mixing with a square law detector (SLD) [6,8], direct signal strength measurement [9] as well as use of a linear receiver with quadrature channels [10–12].

The effect of EM shadowing and reflection can be described by the modern physical theory of diffraction (PTD) developed by Ufimtsev [13] or by the geometrical theory of diffraction [14]; in this chapter, only the PTD is considered. According to the theory, the total scattered field $\vec{E}_{\mathrm{sc}}$ of an object can be described by two constituent fields, the reflected field $\vec{E}_{\mathrm{ref}}$ and the shadow field $\vec{E}_{\mathrm{sh}}$ [15,16],

$$\vec{E}_{\mathrm{sc}} = \vec{E}_{\mathrm{ref}} + \vec{E}_{\mathrm{sh}} \tag{13.2}$$

and are illustrated in Figure 13.2.

The shadow field is so termed because it is most prominent in the spatial regions which are geometrically shielded (shadowed) by the target, i.e. about the axis directly behind the target in the FS direction. The shadow contour (silhouette) defines the geometric boundary between the illuminated and non-illuminated sides of the object.

A full shadow, i.e. zero field intensity, exists only directly behind the object, so-called umbra region, and is referred to as the geometrical shadow, the phenomena that can be described by means of geometrical optics [13 (p.11)]. In this region, the shadow field is interpreted as a field equal to the incident field but having an opposite phase such that the fields sum is equal to zero $\vec{E}_{sc} = \vec{E}_{inc} + \vec{E}_{sh} = 0$. This kind of shadow is usually observed in optics where the wavelength is many orders less than the object dimension. In FSR, the transmitted signal wavelengths are comparable or of order less than target dimensions and due to diffraction effects the illuminating

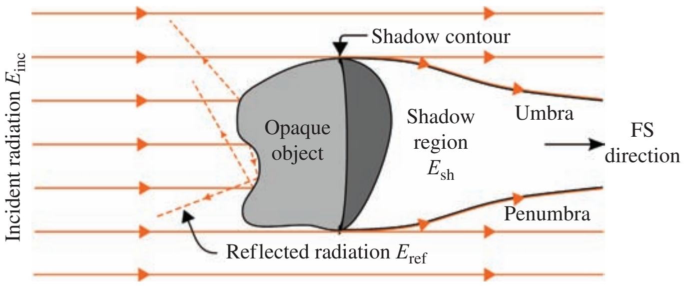

Figure 13.2 Pictorial interpretation of shadow radiation, the shadow field E_{sh} cancels the incident field E_{inc} in regions that are in very close proximity behind the target object

field skirts the obstacles just reducing the strength of the incident field and what is seen behind the object is known in optics as the penumbra. The smaller electrical dimension of the object and the bigger distances between the receiver and the object, the less will be the shadowing effect. In the far field, the shadow field 'on axis' takes the form of a field shifted by $\pi/2$ with respect to the incident field [16]. In [11], the typical ratio between the DPS and the scattered signal levels in the forward direction has been analysed, i.e. the DPS strength modulation due to the target presence in FSR, and this ratio, called signal-to-leakage ratio, was estimated to be -40 to -80 dB.

Summarising from analysis in [13], the shadow field based on the PTD assumptions:

- does not depend on the whole 3D shape of the scattering object and is completely determined by the size and the geometry of the shadow contour (shadow contour theorem).
- is independent of the material properties of the target object assuming of course that this material is not fully transparent for EM waves.

13.2.2 Forward scatter cross-section

When analysing the FS effect, it is worth recalling the mechanisms of EM scattering from objects classified by three regions: optical scattering, where the electrical dimension of the object is large, i.e. geometrical dimension, D, is much greater than the wavelength, λ, $D/\lambda \gg 1$; Mie or resonance region, where $D/\lambda \sim 1$ and, finally, the Rayleigh region where $D/\lambda \ll 1$. In this section, being that the majority of known FSR and related research has been considered in upper Mie and optical region (see Table 13.1), we will consider these cases, but later the Rayleigh region will also be discussed in brief.

In traditional radar, the target echo signal strength is specified by its RCS, σ, for both monostatic radar (σ_m) and bistatic radar (σ_b) cases, which is defined as:

$$\sigma = \lim_{R\to\infty} 4\pi R^2 \frac{|E_{\mathrm{sc}}|^2}{|E_{\mathrm{inc}}|^2}\,[\mathrm{m}^2] \tag{13.3}$$

where E_{inc} and E_{sc} are the electric field strength of the incident wave at the target location and the strength of the scattered electric field in the direction of the observation point correspondingly; R is the target range from the observation point.

In FSR, there is a similar parameter which specifies the signal strength at the receiver – the forward scatter cross-section (FSCS), σ_{fs}, also measured in m^2 or dB m^2.

The FSCS pattern in the Mie and optical region for a target of three-dimensional shape can be calculated by replacing the target with an appropriate plane shape of area A, defined by the shadow contour. This is then replaced by a complementary aperture [19 (p.41)]; the replacement is based on Babinet's principle and is pictorially demonstrated in Figure 13.3.

Table 13.1 EM operational regions of FSR

Reference	Brief description	Frequency (MHz)	Targets	~D/λ	Region
[1 (p.33)]	Radar fences investigated before WWII (Japan)	25–80	Aircraft: 10–20 m of body length	2.0–5.0	Upper Mie/low optical
[2]	Cold war period anti-ballistic missile fences, e.g. AN/FPS 19, AN/FPS 23 (US, Canada)	480–1,350	Long range missiles: 10–20 m	27–75	Optical
[15 (Ch.19)]	Modern anti-stealth Russian radar (RU)	430	Stealth Jet: 10–20 m	20	Optical
[7]	Experimental anti-stealth radar (RU)	900	Fighter Jet: 10–20 m	40	Optical
[17]	Experimental radar for small maritime targets detection	7,000–24,000	Inflatable boat: 3 m	75–225	Optical
[18]	Experimental radar for small ground targets detection	65–430	Typical vehicle, e.g. 4×4: 4 m	1.0–5.0	Mie/upper Mie/lower optical

When the target is directly on the baseline, i.e. $\beta = 180^\circ$, the FSCS tends to its maximum [15 (p.397)],

$$\sigma_{\text{fs}}^{\max} = 4\pi\left(\frac{A}{\lambda}\right)^2 \tag{13.4}$$

coinciding with the monostatic RCS of a flat conductive surface normal to the baseline and with a shape given by the target silhouette with an area A. From (13.4), it is seen that FSCS increases as the fourth power of the target linear size and to a the second power of the carrier frequency. Such rapid increase of forward scattering intensity with frequency is known as the FS effect. At first glance, it highlights advantages of FSR operation at high frequencies; however, the operational frequency choice is actually defined by a number of other parameters considered later.

The monostatic RCS and FSCS of a conductive sphere of radius R_s are shown in Figure 13.4 [20]. It is seen that starting from the Mie region, the mean normalised monostatic RCS does not depend on the wavelength, whereas the FSCS rises by 20 dB/decade. This essential increase in EM scattering in the FS direction has been first derived analytically by Mie [21], and over the years, a large amount of research has been performed in this area both experimentally and theoretically.

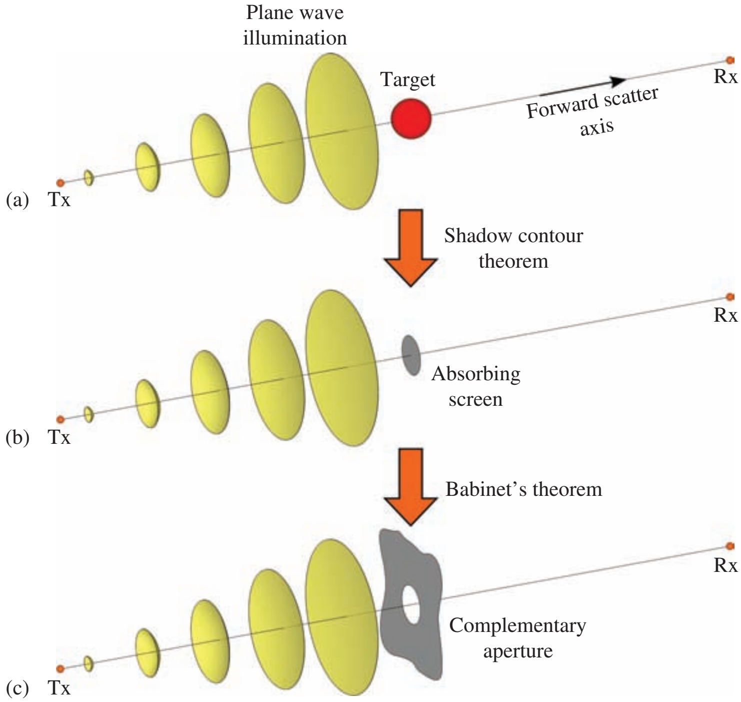

Figure 13.3 Pictorial interpretation of replacement of a complex target with equivalent radiating aperture. (a) Target of a complex 3D shape, (b) equivalent 2D shadow silhouette, (c) silhouette replacement by a complementary aperture in an infinite conductive surface. Wave is planar on incidence with the target

Thus, in the upper Mie and optical region, we may expect $\sigma_{\mathrm{fs}} \gg \sigma_{\mathrm{bs}}$ and $\sigma_{\mathrm{fs}} \gg \sigma_{\mathrm{ms}}$, where $\sigma_{\mathrm{bs/ms}}$ are the bi/monostatic RCSs. To illustrate this further, Table 13.2 shows the estimated improvement in cross-section at different frequencies for typical targets, where the coefficient $\gamma = \sigma_{\mathrm{fs}}/\sigma_{\mathrm{m}}$ is the ratio of the FSCS to its monostatic counterpart.

The physical interpretation of the enhancement of the FSCS in comparison with monostatic RCS follows from the fact that according to the Huygens–Fresnel principle, elementary secondary radiators contribute in phase to a total field at an observation point laying on the baseline if this point is in a far field of the secondary sources. Such a dramatic increase of RCS indicates the main advantage of FSR in improving the radar power budget, meaning that it could be effective for target detection in the case of (i) smaller target size, (ii) larger range to target or (iii) less transmit power. The independence of the FSCS on target material, be it metallic or dielectric, makes this system ideally suited for the detection of stealth targets.

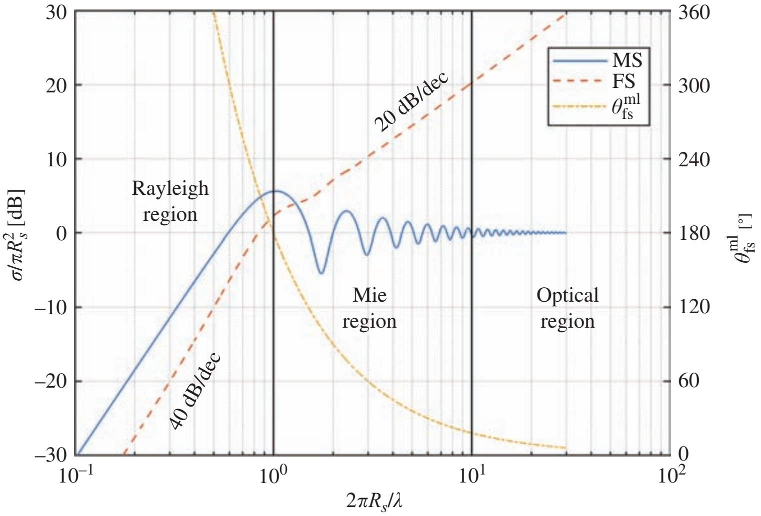

Figure 13.4 Normalised monostatic RCS (labelled MS) and FSCS (labelled FS) of a sphere of radius R_s (left vertical axis) and width of the FSCS main lobe θ_{fs}^{ml} (right vertical axis) [11]

Table 13.2 Comparison of RCS [22 (p.91)] and FSCS for selected targets and frequencies

Carrier frequency (wavelength) [MHz (m)]	**Human 0.5 m^2 RCS A$\sim$1 m^2**	**Vehicle 100 m^2 RCS A$\sim$8 m^2**	**Tank 100 m^2 RCS A$\sim$15 m^2**	**Fighter jet 1 m^2 RCS A$\sim$10 m^2**	**Bomber 10 m^2 RCS A$\sim$40 m^2**	**Small ship 100 m^2 RCS A$\sim$100 m^2**
100 (3)	n/a	n/a	$\gamma = 5$	$\gamma = 21$	$\gamma = 23$	$\gamma = 31$
300 (1)	n/a	$\gamma = 9$	$\gamma = 12$	$\gamma = 28$	$\gamma = 30$	$\gamma = 38$
900 (0.3)	$\gamma = 24$	$\gamma = 19$	$\gamma = 22$	$\gamma = 38$	$\gamma = 40$	$\gamma = 48$
3,000 (0.1)	$\gamma = 33$	$\gamma = 28$	$\gamma = 32$	$\gamma = 47$	$\gamma = 49$	$\gamma = 57$

Equation (13.4) characterises the maximal value of FSCS, another parameter of interest is the FSCS main lobe, which can also be estimated assuming a far-field target/radar configuration. The angular width of the main lobe, $\theta_{\rm fs}^{\rm ml}$, in a certain plane with respect to the target is proportional to the electrical length of the target, i.e. the ratio of the maximal target effective dimension $D_{\rm eff}$ in that plane and the wavelength λ,

$$\theta_{\rm fs}^{\rm ml} = \frac{K\lambda}{D_{\rm eff}}\,[\text{rad}] \tag{13.5}$$

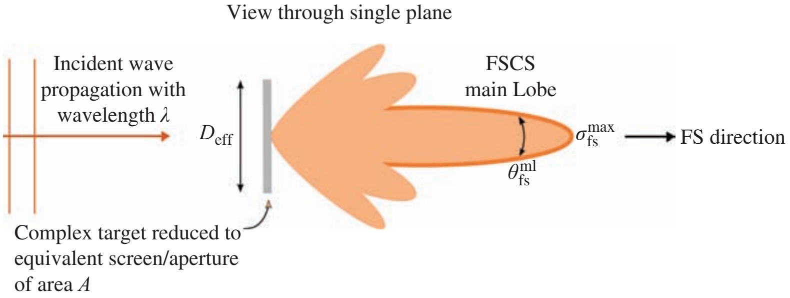

Figure 13.5 Illustration identifying the FSCS main lobe and definitions relating to calculation of the FSCS maximum, σ_{fs}^{max} *and main lobe width,* θ_{fs}^{ml}*, for a complex target which has been reduced to an equivalent screen/aperture*

In general, the coefficient K in (13.5) depends on the actual shadow contour shape but for most practical cases [22 (Ch.12)] $K \approx 1$. For clarity, the illustration in Figure 13.5 identifies the main lobe of the FSCS and the parameters of maximum FSCS, $\sigma_{\mathrm{fs}}^{\mathrm{max}}$ and main lobe width, $\theta_{\mathrm{fs}}^{\mathrm{ml}}$ from (13.4) and (13.5).

Returning to the sphere of radius R_s, the -3 dB width of the FSCS main lobe is shown in Figure 13.4. We can see that the greater the target electrical dimension, the greater its FSCS, σ_{fs} and the narrower is the region defined by $\theta_{\mathrm{fs}}^{\mathrm{ml}}$, where the FSCS enhancement can be observed. The width of main lobe of the FSCS where more than 90% of the received signal energy can be concentrated has a vital role in target detection and tracking, where σ_{fs} defines the radar power budget and, hence, the radar detection performance, $\theta_{\mathrm{fs}}^{\mathrm{ml}}$ specifies the FSR coverage area. It is also worth noting that both $\theta_{\mathrm{fs}}^{\mathrm{ml}}$ and σ_{fs} depend on the wavelength and target dimension and for the simplified case of a target of equivalent aperture area A, defined by an effective dimension, D_{eff}, these two parameters can be combined into one equation which highlights the fundamental relationship between the FSCS and operational area of FSR by substituting (13.5) into (13.4), with an example case of a sphere,

$$\theta_{\mathrm{fs}}^{\mathrm{ml}} \approx \pi\sqrt{\frac{A}{\sigma_{\mathrm{fs}}^{\mathrm{max}}}} \quad \text{or} \quad \sigma_{\mathrm{fs}}^{\mathrm{max}} \approx \frac{A\pi^2}{\left(\theta_{\mathrm{fs}}^{ml}\right)^2} \tag{13.6}$$

In spite of the fact that the first sidelobes of the FSCS pattern carry much less energy in comparison with the main lobe they still play significant role at the stage of target trajectory parameter estimation and importantly in automatic target classification. For airborne targets, the FSCS pattern main and sidelobe widths are also important factors when evaluating the FSR coverage area in elevation in order to determine the maximum altitude of a detectable target.

13.2.2.1 Target visibility time and Doppler resolution in FSR

It follows that if the FSCS main lobe width is known, it is possible to evaluate a target visibility time [11,18] which coincides with the target echo coherence interval $\Delta\tau_{\text{fs}}$. If a target of effective dimension D_{eff} is crossing the baseline at a distance R_r from the receiver with a velocity component, v_{tg}, normal to the baseline, its visibility time T_v at -3 dB level of the FSCS main lobe can be approximated as,

$$T_v = \Delta\tau_{\text{fs}} \approx \frac{\lambda R_r}{2D_{\text{eff}} \cdot v_{\text{tg}}} \tag{13.7}$$

Hence, the potential Doppler (frequency) resolution is:

$$\Delta f_{\text{fs}} = \frac{1}{\Delta\tau_{\text{fs}}} = \frac{1}{T_v} = \frac{2D_{\text{eff}} \cdot v_{\text{tg}}}{\lambda R_r} \tag{13.8}$$

In monostatic radar [15], the target fluctuation spectrum bandwidth Δf_{ms} and corresponding coherency time $\Delta\tau_{\text{ms}} \approx 1/\Delta f_{\text{ms}}$ also depend on the signal wavelength, target effective dimension D_{eff} and target angular variation rate relevant to the radar boresight $d\varphi/dt$, expressed in °/s, through:

$$\Delta f_{\text{ms}} \approx \frac{D_{\text{eff}}}{\lambda} \cdot \frac{d\varphi}{dt} \tag{13.9}$$

Examples of the calculated fluctuation spectra bandwidth Δf_{ms} and the maximum coherent integration time $\Delta\tau_{\text{ms}}$ for an unmanned aerial vehicle (UAV) (wingspan $D = 12$ m) are presented in Table 13.3 [11] for different wavelengths and aspect angle variation rates alongside corresponding FSR parameters.

It can be seen from the table that the Doppler resolution in FSR is several orders better than its monostatic counterpart. This high Doppler resolution defines FSR capabilities such as target tracking, automatic target classification and even imaging [6,15 (Ch.16 & 17), 23].

Table 13.3 Maximum echo coherent time in monostatic radar and FSR for UAV target [11]

	Monostatic						**FSR**	
$\Delta\varphi/\Delta t$	**0.2**		**0.4**		**0.8**		**Baseline = 40 km**	
(°/s) →							v_{tg} **= 50 m/s**	
λ (m) ↓	Δf_{ms}	$\Delta\tau_{\text{ms}}$	Δf_{ms}	$\Delta\tau_{\text{ms}}$	Δf_{ms}	$\Delta\tau_{\text{ms}}$	Δf_{fs}	$\Delta\tau_{\text{fs}}$
3.0	0.8	1.25	1.6	0.63	3.2	0.31	0.013	75
1.5	1.6	0.63	3.2	0.31	6.4	0.16	0.026	37.5
0.75	3.2	0.31	6.4	0.16	12.8	0.09	0.053	18.8
0.3	8.0	0.13	16.0	0.06	32.0	0.03	0.13	7.5
0.1	24.0	0.04	48.0	0.02	96.0	0.01	0.4	2.5
0.03	80.0	0.01	160.0	0.006	320.0	0.003	1.3	0.75

13.2.3 Target FSCS pattern

The full FSCS pattern (as opposed to just the main lobe) can be viewed and analysed as the radiation pattern of the secondary planar antenna. The pattern of an arbitrary aperture antenna is shown in Figure 13.6 where the sidelobes are significantly lower than the main lobe. For some targets, these sidelobes may still exceed the peak levels of RCS of bistatic radar or monostatic radar.

In the figure, $\vec{\rho}$ is a radius vector to point P_A on the aperture, $\vec{r}_0$ is the unit vector towards the evaluation point P and $\vec{R}_p$ is the radius vector to that point, A_{sh} is the area of the aperture. Using the notations and co-ordinates depicted in Figure 13.6, the target FSCS σ_{fs} at bistatic angles close to 180° can be calculated as:

$$\sigma_{fs}(\vec{r}_0) = \lim_{R\to\infty} 4\pi R^2\left(\frac{|E_{sh}|^2}{|E_{inc}|^2}\right) = \frac{4\pi}{\lambda^2}\left|\iint_{A_{sh}} \exp[j(2\pi/\lambda)\vec{\rho}\vec{r}_0]dS\right|^2 \qquad (13.10)$$

where dS is an elementary area of co-phasal aperture A_{sh}. Equation (13.10) fundamentally describes the full FSCS pattern but for complex targets the integration is complex and typically involves numerical full-wave simulation. Modern software packages for full wave analysis, for example CST Microwave Studio [24] may be used for the 3D FSCS pattern analysis.

Prior to discussion of the FSCS pattern it should be stressed that (13.10) describes directional pattern of a shadow aperture of the target, which can be seen as 'black body' radiation, i.e. radiation of an object which absorbs the incident EM wave. The fundamental analogy to this is the ideal 'stealth' target and, therefore, the only way to detect such a target is to use FSR: any detectable scattering on the

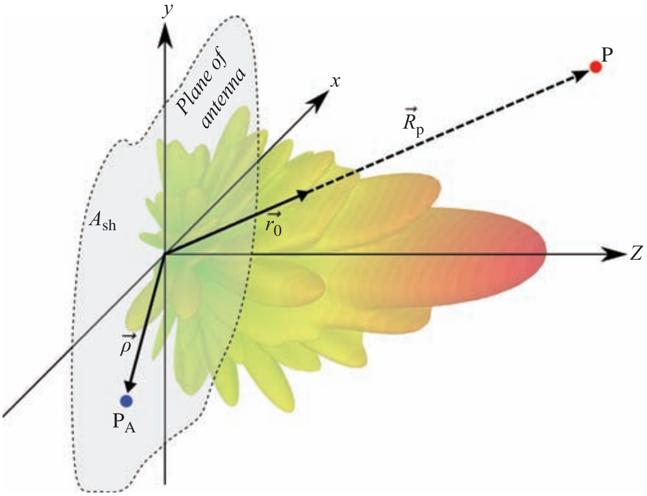

Figure 13.6 The FSCS pattern may be obtained from calculation of an equivalent aperture antenna

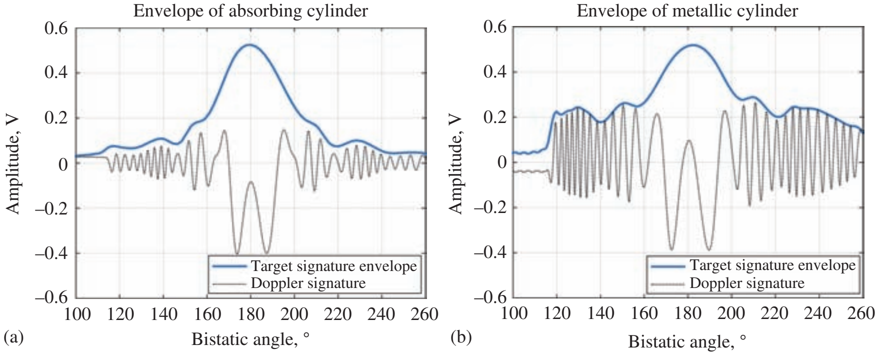

Figure 13.7 Doppler signature and signal envelope (RCS) of (a) a cylinder coated with an absorber and (b) a metal cylinder, as a function of bistatic angle [25]

target shall be attributed to shadowing components even if the target is well outside the baseline. Real targets, even those referred to as ‘stealthy’ only partly absorb the EM waves and at the receiver both reflected (backscattering and bistatic reflection) and shadow (forward scattering) EM waves components are present, as explained in the previous section. Typically, the FS region is associated with the area where forward scattering components of EM waves dominate above bistatic [1 (p.150–155)]. The boundary between the bistatic and FS region is soft, depends on the material and shape and requires EM analysis for each particular target. The only firm statement which can be made without strict analysis is that the FSCS main lobe shadow component always dominates above the bistatic reflected component. It also may be supposed that the ‘stealthier’ the target is the wider will be an area of FS domination that will include not only the FSCS main lobe but also its sidelobes. This effect has been demonstrated in [25] where it has been shown experimentally that the magnitude of signals from two identical metallic cylinders one of which was coated with absorbing material differ in the region of bistatic reflection by approximately 8 dB, while in the FS region, related to the mail lobe, the difference is negligible. The envelopes of two signals at the received signal strength indicator (RSSI) receiver output, corresponding to the RCS of both cylinders as a function of bistatic angle, are shown in Figure 13.7 for cylinders which are (a) absorbing and (b) metallic.

The magnitude of the envelope is significantly larger in the region between about 170° and 190° which corresponds to the FSCS main lobe region. Reflections from the coated cylinder within regions of 120°–170° and 190°–240° are significantly smaller than that of the metallic cylinder and in the case of coated cylinder these regions show mainly FSCS sidelobe levels.

In Figure 13.8(a) results of modelling by PTD for shadow radiation pattern of a cylinder (continuous line) and the total physical optics (PO) radiation pattern (dashed line) are shown, highlighting that the shadow radiation is focussed in the FS direction (45°) [13 (p. 239)]. Figure 13.8(b) shows results of full RCS simulation by

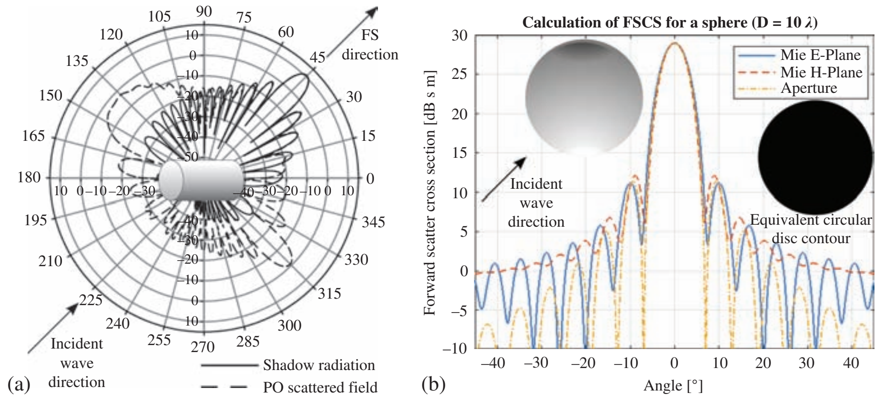

Figure 13.8 The total physical optics scattered far field of (a) cylinder, showing the contribution from shadow radiation which is focussed in the FS direction (45° in this figure) – © [2006] John Wiley and Sons. Reprinted, with permission, from [13] and (b), RCS of sphere simulated according to Mie theory and FSCS from aperture approximation (FS direction is 0°)

Mie theory for a sphere (E and H plane) and FSCS of an aperture approximated as a disc of the same radius (Airy pattern). Clearly, the main and first sidelobes of shadow field/FSCS in these examples dominate above other scattering components.

In [11], the 3D RCS for a side illuminated missile were simulated in CST Microwave Studio at two frequencies of 100 MHz and 1 GHz, corresponding to the upper Rayleigh-low Mie scattering mechanism and optical scattering regions respectively – Figure 13.9(a) and (b). The azimuth plane cross-sections are shown in Figure 13.9(c) and (d). Illumination occurs such that in the figure, the backscattering direction is 0° azimuth and FS corresponds to 180° azimuth angle. For the target length of 3.6 m and the wavelength of 3 m (Rayleigh–Mie region), there are two well-defined maxima of back and forward scattering lobes: 11.7 and 9 dB s m, respectively. This confirms the fact that in the case where the effective size of the object is comparable to the wavelength, the backscattering and forward scattering are of approximately the same intensity. For the same target, illuminated by a 0.3 m wavelength signal, corresponding to the optical scattering region, there are also two pronounced maxima for back and forward scattering, but both lobes are very narrow, of the order of a few degrees, their maximum intensity is greater than for the Rayleigh–Mie case, and the FSCS main lobe is approximately 10 dB greater than that of the backscattering lobe. In the bistatic (side) scattering direction, with azimuth angular ranges away from forward and backscatter and centred around 90° and 270°, the RCS drops by up to 30–35 dB relative to the FS. Assuming that the missile is 'stealth' shaped or coated for monostatic radar, the pronounced peak in backscatter direction will be absent, and the target is likely to be detected only in the FS region.

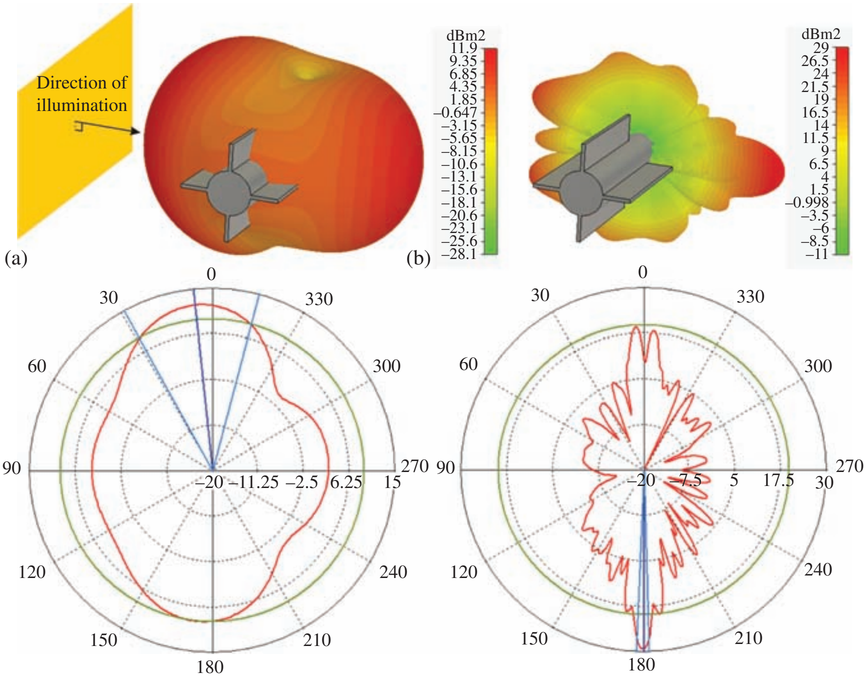

(c) Azimuth angle (°) vs. RCS (dB m^2)

(d) Azimuth angle (°) vs. RCS (dB m^2)

Figure 13.9 Simulated 3D bistatic RCS for missile [11] with (a) 3 m wavelength and (b) 0.3 m wavelength with their corresponding cross-sections (c) and (d). Backscattering angle is 0°, FS angle is 180°

In the same paper, CST Microwave Studio simulation of RCS has been performed for a number of typical targets (shown in Figure 13.10) in order to estimate level of bistatic reflections, where the bistatic angle $\beta = \pi/2$, and forward scattering $(\beta = \pi)$ at several frequency bands. Results are summarised in Table 13.4, where frequency bands refer to different scattering mechanisms: Rayleigh (R), Mie (M) and Optical (O). As it can be seen from this table, the significantly larger RCS in FS direction is observed for all cases of Mie and optical scattering. For instance, two targets – a UAV and a 3.6 m long missile, have FSCS of 33 dB m^2 and 23 dB m^2 accordingly at 400 MHz (0.75 m wavelength) – the frequency which is well suited for air target detection. Even without deep analysis, it is seen that these numbers provide an excellent power budget in FSR which are 20–30 dB above the bistatic RCS at 90°.

As was mentioned above for the detailed structure of FSCS pattern is important for the target recognition and imaging in FSR. However, for the majority of radar tasks and to see the general effects of target dimension on radar performance, particularly in terms of radar power budget, we can use rather simple approximation of the target RCS by replacing the target silhouette by a rectangle [26] or composition of rectangles which can be used to approximate any target shadow aperture and has simple and well-known pattern from antenna theory

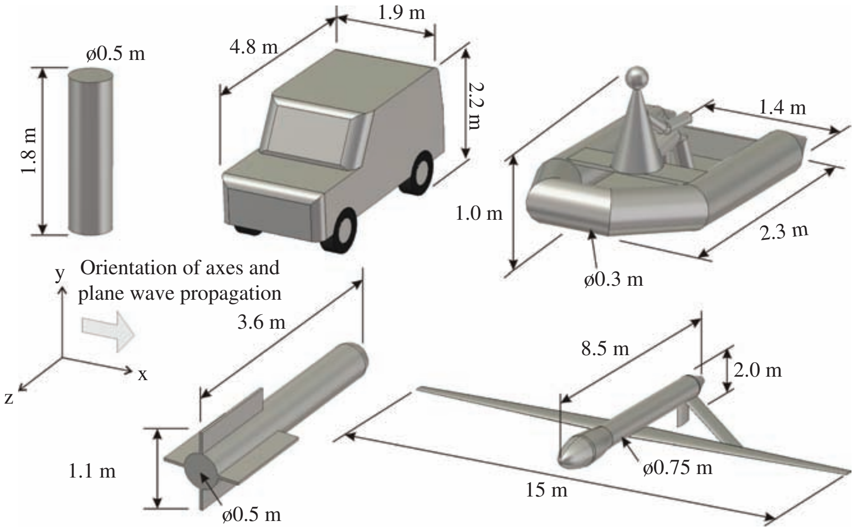

Figure 13.10 Target shapes and dimensions for 3D RCS simulations of which results are shown in Table 13.4 (illumination from left side as shown) [11]

Table 13.4 Bistatic RCS vs FSCS for a selection of targets [11]

	RCS, dB s m				
	Bistatic radar ($\beta = 90°$)/FSR ($\beta = 180°$)				
$\lambda \rightarrow$	3.0 m	1.5 m	0.75 m	0.3 m	0.1 m
$f \rightarrow$	100 MHz	200 MHz	400 MHz	1 GHz	3 GHz
Targets, *L* (m), *H* (m), *V*(m/s)					
Human $L = 0.5$, $H = 1.8$, $V = 1.0$	6.2/7.6 (R)	7.3/11.1 (M)	7.6/15.6 (M)	11.6/22.0 (O)	15.4/33.2 (O)
Vehicle, 4×4 $L = 4.8$, $H = 2.2$, $V = 10$	9.7/22.5 (R/M)	7.6/28.2 (M)	−7.4/34.1 (sub-O)	5.4/41.0 (O)	–
Inflatable boat $L = 2.3$, $H = 1$, $V = 5$	0.6/2.7 (R)	−1.3/6.8 (M)	−9.4/13.0 (Sub-O)	−6.6/21.4 (O)	−7.3/40.3 (O)
Missile $L = 3.6$, $H = 0.5$, $V = 200$	2.9/8.9 (R/M)	1.6/15.3 (M)	−8.0/22.6 (Sub-O)	−6.1/29.0 (O)	−3.2/45.0 (O)
UAV $L = 8.4$, $H = 2$, $V = 50$	4.4/17.6 (M)	2.0/23.5 (O)	−1.6/32.9 (O)	−3.0/60.0 (O)	–

[22 (p.584–602)]. Figure 13.11(a) graphically defines the shadow aperture as an effective aperture projected onto the plane normal to the illuminating wave direction, with effective area A_{eff} and length l_{eff}. With the notation of Figure 13.11(b), the 3D FSCS of the rectangular secondary antenna representing

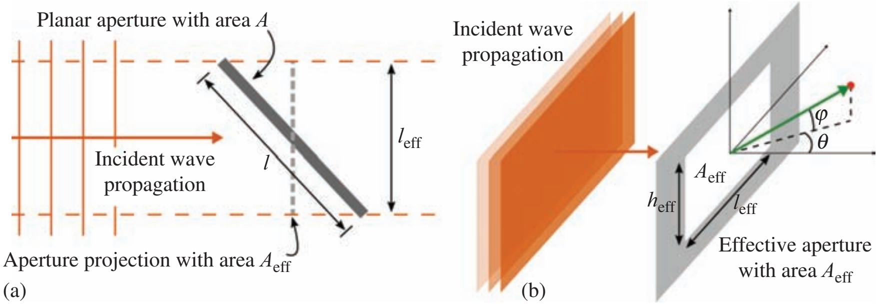

Figure 13.11 Effective shadow aperture as a projection of the shadow contour onto the plane normal to the incident wave direction (a) – for clarity the aperture is shown as solid; the co-ordinate system and variables defined for FSCS calculation are shown in (b)

shadow contour of the target is expressed as a function of the two angles specifying the direction of scattering:

$$\sigma_{\text{fs}}(\theta,\varphi) = 4\pi\frac{{A_{\text{eff}}}^2}{\lambda^2}\left(\frac{\sin((\pi l_{\text{eff}}/\lambda)\sin\theta)}{(\pi l_{\text{eff}}/\lambda)\sin\theta}\right)^2\left(\frac{\sin((\pi h_{\text{eff}}/\lambda)\sin\varphi)}{(\pi h_{\text{eff}}/\lambda)\sin\varphi}\right)^2 \qquad (13.11)$$

This simple method of replacing a complex shape target by an equivalent rectangular plate is very convenient for looking at generalised system behaviour and will be used further in this chapter.

13.3 Power budget, signature of moving target and optimal signal processing in FSR

13.3.1 Power budget analysis

The power budget analysis for FSR [28–30] has a lot in common with both monostatic [30] and bistatic radar [1]. There are two basic models of EM wave propagation: the free space model and two-ray path (TRP) propagation model which are shown in Figure 13.12(a) and (b) accordingly.

The free space propagation model is applicable for the cases: (i) the height of the antennas is comparable to the separation distance between Tx and Rx; (ii) the radar antennas have a rather narrow main beam (shown as shaded areas in Figure 13.12) and do not illuminate the surface below; (iii) the surface roughness is comparable with the wavelength which results in dominant diffused scattering by the potentially reflecting surface so that there is no single ground specular reflected beam contributing into the total field at the receiver input [17]. In contrast with the two-ray model, the reflected signal may have the same order of magnitude as the DPS but the total field will depend on the phase relationship between them.

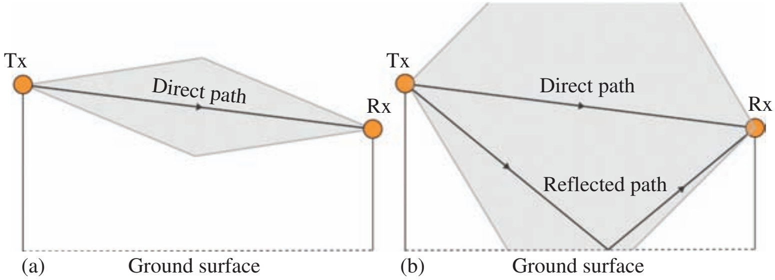

Figure 13.12 Configuration for (a) free space propagation model and (b) two-ray path propagation model when antenna beam intersects the ground

13.3.1.1 Free space propagation model

In FSR, two signals contribute into the total received power and power of each must be individually estimated; the power of leakage (which in the case of the free space model is the DPS), $P_{\mathrm{dp}}^{\mathrm{fsp}}$, and power of the signal scattered from the target, $P_{\mathrm{tg}}^{\mathrm{fsp}}$, where ‘fsp’ stands for free space propagation, ‘dp’ is for the direct path (leakage) signal (Figure 13.12) and ‘tg’ is for the target signal. The power of the LS can be estimated by the Friis equation [31 (pp.16–18)] which can be presented in one of the following forms:

$$P_{\mathrm{dp}}^{\mathrm{fsp}} = P_t G_t G_r \left(\frac{\lambda}{4\pi d}\right)^2 \frac{1}{L} = \frac{P_t}{4\pi d^2}\frac{G_t A_r}{L} = \frac{P_t G_t G_r}{L_p L} \tag{13.12}$$

where P_t, G_t, G_r are the transmit power, gains of transmit and receive antennas, correspondingly, A_r is the effective area of the receive antenna, d is the direct path/baseline length, L_P is the propagation loss and L represents the miscellaneous losses which are always present in real systems and environments.

To estimate $P_{\mathrm{tg}}^{\mathrm{fsp}}$, the bistatic radar equation can be used, where FSCS, σ_{fs} is used instead of the bistatic RCS:

$$P_{\mathrm{tg}}^{\mathrm{fsp}} = \frac{P_t G_t G_r \lambda^2 \sigma_{\mathrm{fs}}}{(4\pi)^3 R_t^2 R_r^2 L_{\mathrm{tg}}} \tag{13.13}$$

and where L_{tg} are the other losses as in (13.12), but in the presence of the target. According to (13.13), $P_{\mathrm{tg}}^{\mathrm{fsp}}$ reaches a minimum when the transmitter/receiver-to-target ranges are equal, i.e. $R_t = R_r = d/2$ and the radar range equation in this case will take the form:

$$d_{\max}^{\mathrm{fsp}} = 2\sqrt[4]{\frac{P_t G_t G_r \sigma_{\mathrm{fs}} \lambda^2}{(4\pi)^3 S_{\min} L_{\mathrm{tg}}}} \tag{13.14}$$

where $S_{\min}$ is the minimal required detectable signal level corresponding to a particular signal-to-noise ratio (SNR).

In many situations, it is convenient in FSR to consider the ratio of the target signal and the LS, that is:

$$\frac{P_{\mathrm{tg}}^{\mathrm{fsp}}}{P_{\mathrm{dp}}^{\mathrm{fsp}}} = \frac{d^2\sigma_{\mathrm{fs}}}{4\pi R_t^2 R_r^2} \tag{13.15}$$

where for a simplicity the miscellaneous loss factors are omitted, but readers should always remember them.

Equation (13.13) looks very similar to its bistatic radar counterpart but in practice has a very important peculiarity which is not only due to essentially bigger RCS. The peculiarity lies where the FSCS is coupled with the system wavelength in the optical region which introduces some restriction in FSR. To demonstrate this, let us first replace σ_{fs} in (13.13) by its maximal value $\sigma_{\mathrm{fs}}^{\max}$ according to (13.4) and assume that the target has a rectangular shadow silhouette of length l_{eff} and height h_{eff} (Figure 13.11), so that:

$$\sigma_{\mathrm{f}s}^{\max} = 4\pi\left(\frac{l_{\mathrm{eff}}h_{\mathrm{eff}}}{\lambda}\right)^2 \tag{13.16}$$

Equation (13.13) thus transforms into

$$P_{\mathrm{tg}}^{\mathrm{fsp}} = \frac{P_tG_tG_r\lambda^2}{(4\pi)^3R_t{}^2R_r{}^2}\cdot 4\pi\left(\frac{l_{\mathrm{eff}}\cdot h_{\mathrm{eff}}}{\lambda}\right)^2 = \frac{P_tG_tG_r(l_{\mathrm{eff}}\cdot h_{\mathrm{eff}})^2}{(4\pi)^2R_t{}^2R_r{}^2} \tag{13.17}$$

which leads to the conclusion that the power of the received signal in FSR does not depend on the carrier frequency, assuming fixed antenna gains.

It is worth recalling here that the required radar performance is ultimately specified by the SNR. The output of an optimal receiver, which is based on a correlator or matched filter, is specified by the energy of the received signal E_{r} normalised to the noise power spectral density (PSD) N_0 as $\mathrm{SNR}_{\mathrm{out}} = 2E_r/N_0$ [33 (p.280)]. Assuming a constant signal power during the observation time $\Delta\tau_{\mathrm{fs}}$, which itself depends on the wavelength as follows from (13.7), the output SNR is:

$$\mathrm{SNR}_{\mathrm{out}}^{\mathrm{fsp}} = \frac{2P_{\mathrm{tg}}^{\mathrm{fsp}}\Delta\tau_{\mathrm{fs}}}{N_0} = \frac{P_{\mathrm{tg}}^{\mathrm{fsp}}\lambda R_r}{l_{\mathrm{eff}}v_{\mathrm{tg}}N_0} \tag{13.18}$$

The notation in this equation corresponds to that of (13.8). Now by combining (13.18) and (13.17):

$$\mathrm{SNR}_{\mathrm{out}}^{\mathrm{fsp}} = \frac{P_tG_tG_rh_{\mathrm{eff}}{}^2l_{\mathrm{eff}}\lambda}{(4\pi)^2R_t^2R_rN_0v_{\mathrm{tg}}} = \frac{P_tA_tA_rh_{\mathrm{eff}}{}^2l_{\mathrm{eff}}}{\lambda^3R_t^2R_rN_0v_{\mathrm{tg}}} \tag{13.19}$$

where A_t, A_r are the effective areas of the transmit and receive antennas. Equation (13.19) gives an insight into how the FSR radar parameters affect the system performance for a required SNR, which is inversely proportional to the target-to-receiver range and the square of the transmitter-to-target range. Also it is proportional to the square of the target vertical dimension but linearly related to its length.

While the power in (13.13) reaches its minimum at $R_t = R_r$, (13.19) reaches its minimum at $R_r \approx 0.33d, R_t \approx 0.67d$ and hence the minimum of the SNR will be:

$$\mathrm{SNR}^{\mathrm{fsp}}_{\mathrm{out,\ min}} = \frac{P_t G_t G_r {h_{\mathrm{eff}}}^2 l_{\mathrm{eff}} \lambda}{0.15(4\pi)^2 d^3 N_0 v_{\mathrm{Tg}}} \tag{13.20}$$

Therefore, the maximum detection range/baseline length $d^{\mathrm{fsp}}_{\mathrm{max}}$ considering the maximum target observation time as defined in Section 13.2.2.1 is:

$$d^{\mathrm{fsp}}_{\mathrm{max}} \approx \sqrt[3]{\frac{P_t G_t G_r {h_{\mathrm{eff}}}^2 l_{\mathrm{eff}} \lambda}{0.15(4\pi)^2 SNR^{\mathrm{fsp}}_{\mathrm{out,\ min}} N_0 v_{\mathrm{tg}}}} \tag{13.21}$$

The noise PSD can be evaluated as $N_0 = kT \cdot N_f$, where the Boltzmann constant $k = 1.38 \cdot 10^{-23}\ J/K$, T is the receiver temperature and N_f is the noise factor. As an example let us evaluate the maximal baseline for detection of a UAV target (Figure 13.10) flying with a speed of 50 m/s normal to the baseline assuming a noise figure of $N_f = 6$ dB, antenna gains of $G_t = G_r = 6$ dB (corresponding to a single patch antenna), $P_t = 10$ dBW and other losses (not shown in (13.21)) totalling 20 dB. The results of calculation of the maximal baseline for detection over a range of minimum output SNRs at three frequencies are presented in Figure 13.13.

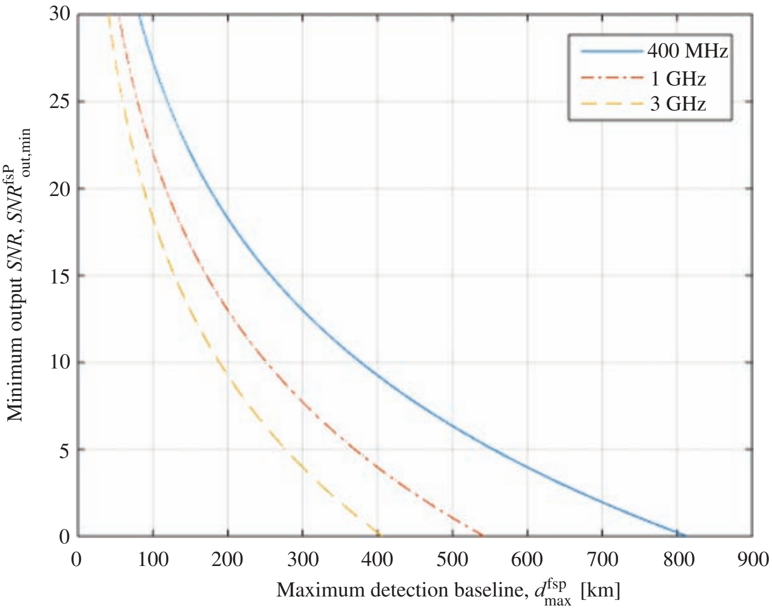

Figure 13.13 Small airborne target maximum detection range (baseline length) in FSR as a function of SNR at three carrier frequencies (free space model)

These numbers, which may seem somewhat excessive, reflect the benefit of a high FSCS and a very long integration time – of the order of seconds for the considered cases. However, it is not likely that such a long integration time can be used in practice. Moreover, it is also important to stress here that at least for a terrestrial system the line-of-sight is rarely present to provide the DPS at the receiver at such a range which is a compulsory condition for FSR operation. In [15 (Ch.19)], an operational FSR with the transmit power of 6 dBW and antenna gains of 18 dB for low-altitude air targets detection and tracking is discussed.

13.3.1.2 Power budget in two-ray path propagation model

In contrast to the free space propagation model, the TRP model takes into account the reflection of the transmitted signal from the surface of land or sea. This model has been developed, comprehensively analysed and well proven experimentally as a part of wireless communication studies, which were reported in numerous papers and books, including the classic book of Kerr [33 (Ch.5)], as well as in radar-related research [31] where the influence of a surface reflection on radar performance has been investigated. For FSR, appropriate material can be found in [28,34].

We will start with a brief description of the TRP model. If the transmitted wave is propagating above the surface, there are two signals (rays) at the reception point, the vector sum of which form a new LS, $E_{\mathrm{lkg}}^{\mathrm{trp}}$. Its magnitude depends on the amplitudes and mutual phase of the two signals; one signal follows the shortest path between the transmitter and the receiver and as in the free space case is referred to as the DPS with electric field strength E_{dp}; the second one is a signal reflected from the surface, E_{ref}– both paths are highlighted in Figure 13.12(b). The latter is a delayed version of the DPS and has a phase shift which depends on the path difference between the two, as well as on the Fresnel reflection coefficient at the air-surface interface, Γ, which in the general case is a complex value. The reflection coefficient depends on the grazing angle, wave polarisation, electrical properties of the surface as well as its roughness and, therefore, the effective reflection coefficient [35] may be used for a rough surface to relax the strict requirement of negligible roughness in the conventional ground reflection model. The amplitude of the combined signal is

$$\vec{E}_{\mathrm{lkg}}^{\mathrm{trp}} = \vec{E}_{\mathrm{dp}} + \vec{E}_{\mathrm{ref}} = \left|\vec{E}_{\mathrm{dp}}\right| \mathrm{e}^{-ikR_{\mathrm{dp}}} + \left|\vec{E}_{\mathrm{ref}}\right| \cdot \Gamma \mathrm{e}^{-ikR_{\mathrm{ref}}} \tag{13.22}$$

where R_{dp} and R_{ref} are the direct path and reflected path distances accordingly. The phase of Γ depends mainly on the surface electrical properties, i.e. electric conductivity and permittivity and grazing angle, while the magnitude depends mainly on the surface roughness. It was shown in a conventional ground reflection model [36 (pp.120–125)], that under the conditions of (i) the ground being smooth with respect to the wavelength and (ii) the heights of the transmit/receive antennas being much smaller than their separation distance, the reflection coefficient does not depend on the wave polarisation and is equal to -1, which is equivalent to the reflection from a flat surface of a perfect conductor where we can expect the maximum signal strength reduction. This extreme approximation nevertheless is very practical as a reference model for the more general case where the surface roughness and electrical properties are unknown *a priori* and depend on presence of vegetation, weather conditions, rain, snow, etc. for land-based radar while for radar operating above the sea surface, it will depend on sea state conditions.

For such a reference model, the LS power at the receiver can be calculated according to:

$$P_{\mathrm{lkg}}^{\mathrm{trp}} = 4P_tG_tG_r\left(\frac{\lambda}{4\pi d}\right)^2\sin^2\left(\frac{2\pi h_th_r}{\lambda d}\right) \tag{13.23}$$

where $h_{t/r}$ are the antenna heights and other parameters have been previously defined. At very low grazing angles this tends to:

$$P_{\mathrm{lkg}}^{\mathrm{trp}} = P_tG_tG_r\left(\frac{h_th_r}{d^2}\right)^2 \tag{13.24}$$

Following the same approach, the power scattered from a target can also be evaluated [34]. In this case, the TRP propagation model should be used on both paths: transmitter-to-target and target-to-receiver as in Figure 13.14(a):

$$P_{\mathrm{tg}}^{\mathrm{trp}} = 16P_tG_tG_r\sigma_{\mathrm{fs}}\frac{1}{{R_t}^2{R_r}^2}\frac{\lambda^2}{(4\pi)^3}\sin^2\left(\frac{2\pi h_tz_{\mathrm{tg}}}{\lambda R_t}\right)\sin^2\left(\frac{2\pi h_rz_{\mathrm{tg}}}{\lambda R_r}\right) \tag{13.25}$$

where z_{tg} is the altitude of a point like target. Then, for near zero grazing (13.25) can be reduced to:

$$\begin{aligned} P_{\mathrm{tg}}^{\mathrm{trp}} &= 16P_tG_tG_r\sigma_{\mathrm{fs}}\frac{1}{{R_t}^2{R_r}^2}\frac{\lambda^2}{(4\pi)^3}\left(\frac{2\pi h_tz_{\mathrm{tg}}}{\lambda R_t}\right)^2\left(\frac{2\pi h_rz_{\mathrm{tg}}}{\lambda R_r}\right)^2 \\ &= P_tG_tG_r\sigma_{\mathrm{fs}}\frac{4\pi}{\lambda^2}\left(\frac{h_tz_{\mathrm{tg}}}{{R_t}^2}\right)^2\left(\frac{h_rz_{\mathrm{tg}}}{{R_r}^2}\right)^2 \end{aligned} \tag{13.26}$$

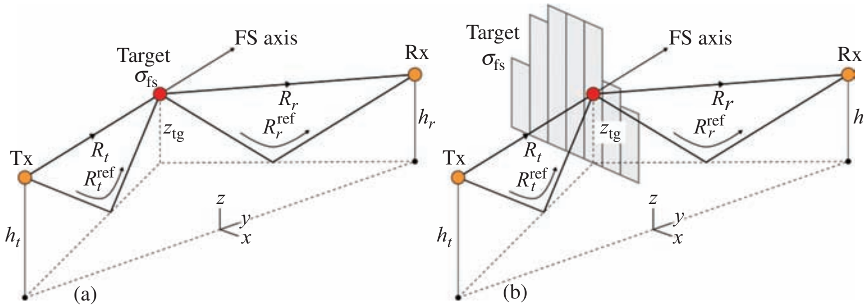

Figure 13.14 Two-ray propagation model for target in FSR considered as (a) a point target and (b) an extended target as composition of strips

In [34], analysis of leakage power and scattered power for a sphere target moving above the ground has been presented, which has demonstrated excellent agreement between that predicted by the TRP model and measured values.

Equation (13.26) can be applied for power budget estimation of a low flying target if its dimensions are smaller than the target altitude z_{tg}, thus acting as a point-like target.

For the case of an extended target, it can be presented as a composition of vertical strips spanning the area of a real target, where z_{tg} will now be defined for the centre point of each strip – Figure 13.14(b). Scattering from each strip of the target could be calculated by (13.26), and the overall received signal power will be a sum of powers scattered from these elementary parts. Further refinement of the model for an extended target should lead to the target aperture being presented by a set of secondary radiators positioned at the centres of elementary rectangular areas of approximately half-wavelength by half-wavelength dimension. This representation is valid when target, transmitter and receiver are in the far field with respect to each other. Thus, the received signal will be the vector sum of fields scattered by each point-like radiator across the shadow aperture of a target [12], power can then be calculated from the received field.

One simplified method involving direct summation of powers has been proposed in [37 (Ch.9)] with application for a maritime monostatic radar. This method will be valid if the target occupies any single Fresnel zone. In this work, the target aperture has been divided into elementary horizontal strips of equal area and the RCS of each part was σ_{fs}/N. The received power from all elementary areas will be the sum of the contributions from each area numbered $1 \le n \le N$:

$$P_{\mathrm{tg}}^{\mathrm{trp}} = \sum_{n=1}^{N} P_t G_t G_r \sigma_{\mathrm{fs}} \frac{4\pi}{N\lambda^2} \left(\frac{h_t z_{\mathrm{tg}}(n)}{R_t(n)^2} \right)^2 \left(\frac{h_r z_{\mathrm{tg}}(n)}{R_r(n)^2} \right)^2 \tag{13.27}$$

where $R_t(n)$ and $R_r(n)$ are ranges to the centre of mass of each elementary strip. When the number of partial areas $N \to \infty$, the sum in (13.27) becomes an integral. This integral could be calculated analytically under some simplifying assumptions but there is a relatively simple rule of thumb which can be used in practice which leads to a rather accurate result in power budget calculation at least for small surface targets such as cars, boats, animals etc. For such targets, (13.25) and (13.26) can be used with the assumption:

$$z_{\mathrm{tg}} \approx 0.5 h_{\mathrm{eff}} \tag{13.28}$$

where h_{eff} is the effective height of the planar target equivalent aperture. This rule has been successfully applied and experimentally confirmed in [34,38,39]. Thus, for surface targets, from (13.26), one can use following equation,

$$P_{\mathrm{tg}}^{\mathrm{trp}} = P_t G_t G_r \sigma_{\mathrm{fs}} \frac{4\pi}{\lambda^2} \left(\frac{0.5 h_t h_{\mathrm{eff}}}{R_t{}^2} \right)^2 \left(\frac{0.5 h_r h_{\mathrm{eff}}}{R_r{}^2} \right)^2 \tag{13.29}$$

Following the methodology which has been used to derive (13.18)–(13.21), but now using the TRP model, the equation for the SNR, $\mathrm{SNR}_{\mathrm{out}}^{\mathrm{trp}}$, at the optimal receiver output will take the form:

$$\mathrm{SNR}_{\mathrm{out}}^{\mathrm{trp}} = \frac{\pi^2 P_t G_t G_r\, h_t^2 h_r^2 l_{\mathrm{eff}} {h_{\mathrm{eff}}}^6}{\lambda^3 v_{\mathrm{tg}} R_t^4 R_r^3 N_0} \tag{13.30}$$

This equation has a minimum when $R_t \approx 0.55d$ and $R_r \approx 0.45d$ and is approximately equal to:

$$\mathrm{SNR}_{\mathrm{out,\ min}}^{\mathrm{trp}} \approx \frac{120\pi^2 P_t G_t G_r\, h_t^2 h_r^2 l_{\mathrm{eff}} {h_{\mathrm{eff}}}^6}{\lambda^3 v_{\mathrm{tg}} d^7 N_0} \tag{13.31}$$

the maximal baseline could then be evaluated as:

$$d_{\max}^{\mathrm{trp}} \approx \left(\frac{120\pi^2 P_t G_t G_r\, h_t^2 h_r^2 l_{\mathrm{eff}} {h_{\mathrm{eff}}}^6}{\lambda^3 v_{\mathrm{tg}} \mathrm{SNR}_{\mathrm{out,\ min}}^{\mathrm{trp}} N_0} \right)^{1/7} \tag{13.32}$$

As an example, let us estimate the maximal baseline for a target representing a 4×4-type vehicle of $l_{\mathrm{eff}} = 5$ m, $h_{\mathrm{eff}} = 2$ m, moving with a speed of 10 m/s normal to the baseline, where both antenna heights are $h_t = h_r = 1$ m. Assuming again that $P_t = 10$ dB W, $N_f = 6$ dB, $G_t = G_r = 6$ dB and other unaccounted losses are 20 dB, for a required $\mathrm{SNR}_{\mathrm{out,\ min}}^{\mathrm{trp}} = 13$ dB the calculated max baseline will be ≈ 1.4 km for 400 MHz. The results of calculation of the maximal baseline for detection over a range of SNRs at three frequencies are presented in Figure 13.15, under the assumption of a flat Earth.

Comparison of the results shown in Figures 13.13 and 13.15 demonstrates the essential difference between free space and TRP propagation model scenarios used in FSR in terms of the power budget dependence on frequency. This corresponds well to a case of ground monostatic radar reported in [31].

13.3.2 Target signature in FSR

The basic physical principle of FSR is the shadowing of the DPS by an object when it occurs in a vicinity of the baseline. In Section 13.2.2, it was stated and discussed that the target FSCS is the key parameter which defines the intensity of the shadowing, i.e. amplitude of modulation of the DPS at FSR receiver input due to target presence. Due to the target motion with respect to transmitter and receiver, the received signal in FSR is a specific waveform and the target signature is formed as a super-position of the incident EM field i.e. LS and the shadow radiation from the moving scattering object – the target.

We can assume that the target follows a linear trajectory with constant speed while its FSCS main lobe is directed towards the receiver. This is generally true for the majority of practical applications [11,40]. Shadow radiation is cast upon the receiver according to the width of the shadow lobe while the target moves in

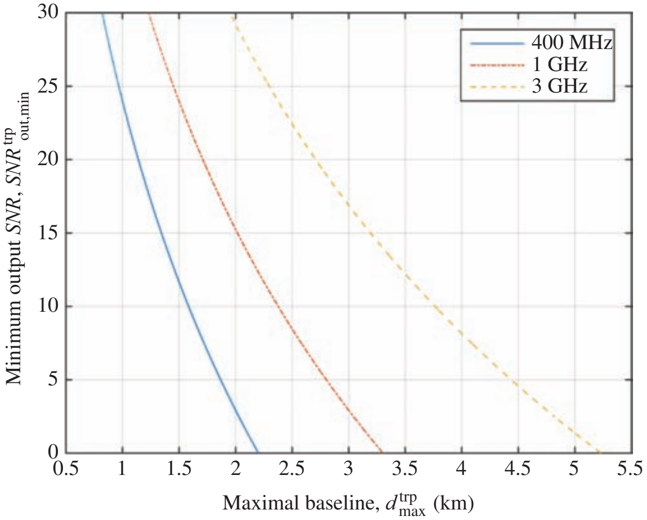

Figure 13.15 4×4 vehicle maximum detection range (baseline length) in FSR as a function of SNR at three carrier frequencies (two-ray path model)

the vicinity of the baseline. The maximum of the shadow radiation corresponds to the case when the target is on the baseline.

13.3.2.1 Phase signature

Let us initially consider a point-like target, which yet casts a shadow on the receiver, and omit any amplitude modulation of the signal caused by propagation loss and by the FSCS pattern, focussing purely on the phase signature of such moving point [11,20,25,41]. Since it is composed of 'shadow radiation', the forward scattered signal is $\pi/2$ phase shifted (imaginary along the FS axis) relative to the LS [43]. Therefore, at the receiver input, a composite signal of the DPS $S_{\text{dp}}(t)$ with an amplitude A_{dp} and delayed scattered signal $S_{\text{tg}}(t)$ from the moving target with amplitude $A_{\text{tg}}(t)$ is acquired,

$$S_r^{\text{in}}(t) = S_{\text{dp}}(t) + S_{\text{tg}}(t) = A_{\text{dp}}\cos(\omega_0 t) + A_{\text{tg}}(t)\sin\left[\omega_0\left(t + \Delta t_{\text{tg}}(t)\right)\right] \tag{13.33}$$

where ω_0 is the carrier angular frequency and $\Delta t_{tg}(t)$ is the delay time of the signal from the moving target with respect to the direct path, given by:

$$\Delta t_{\text{tg}}(t) = \frac{R_t(t) + R_r(t) - d}{c} \tag{13.34}$$

where, as defined previously, $R_{t/r}$ are the transmitter/receiver to target ranges, d is the baseline length and c is the speed of light. The initial phases of coherently acquired signals can be omitted without loss of generality.

To extract the Doppler phase signature component, we will consider a principle based on a self-mixing heterodyne receiver as in [11]. The basis of this mixer is a double-sided SLD, followed by a low-pass filter (LPF) of which the bandwidth is defined by the range of Doppler frequencies expected in the signature [15,38]. Thus, the action upon the signal at the receiver input (13.33) will be,

$$\begin{aligned} &S_r^{\text{in}}(t) \xrightarrow{\text{SLD}} \left[A_{\text{dp}}\cos(\omega_0 t) + A_{\text{tg}}(t)\sin\left[\omega_0\left(t + \Delta t_{\text{tg}}(t)\right)\right]\right]^2 \xrightarrow{\text{LPF}} \\ &DC - A_{\text{ph}}(t)\sin\left(\omega_0 \Delta t_{\text{tg}}(t)\right) = DC - A_{\text{ph}}(t)\sin\left(\frac{2\pi\left(R_{\text{t}}(t) + R_{\text{r}}(t) - d\right)}{\lambda}\right) \end{aligned} \tag{13.35}$$

where $DC = \left(\left(A_{\text{dp}}^2 + A_{\text{tg}}^2\right)/2\right) \overset{A_{\text{tg}} \ll A_{\text{dp}}}{\approx} \left(A_{\text{dp}}^2/2\right)$ is the power of the DPS, $A_{\text{ph}} = A_{\text{dp}}A_{\text{tg}}$ characterises the amplitude of the phase signature. In terms of Doppler shift,

$$S_r^{\text{in}}(t) \xrightarrow{\text{SLD}} \left[A_{\text{dp}}\cos(\omega_0 t) + A_{\text{tg}}(t)\sin((\omega_0 + \omega_d)t)\right]^2 \xrightarrow{\text{LPF}} DC + A_{\text{ph}}(t)\sin\left(\omega_d t\right) \tag{13.36}$$

where ω_d is the angular Doppler frequency shift of the moving target.

Thus,

$$\omega_d t \equiv -\frac{2\pi}{\lambda}\left(R_t(t) + R_r(t) - d\right) + 2\pi n \tag{13.37}$$

where n is an integer, and the last term can be omitted without loss of generality. After removing the leakage (*DC*) component in (13.36), the target Doppler signature extracted at the receiver output is:

$$S_r^{\text{out}}(t) = A_{\text{dp}}A_{\text{tg}}(t)\sin\left[\frac{2\pi}{\lambda}\left(R_t(t) + R_r(t) - d\right)\right] \tag{13.38}$$

For a target crossing the baseline, the phase signature is a two-sided chirp signal, this is well known in radar as a waveform with a good auto-correlation property [43]. An example of this signature and its auto-correlation function are shown in Figure 13.16(a) and (b) correspondingly. This property will be further discussed as a way of target resolution when they follow in a convoy – Section 13.3.3.2.

13.3.2.2 The signature envelope

Following from (13.38), the FS signature could be viewed as a waveform which has frequency (phase) modulated harmonic carrier specified by the Doppler effect and the target motion parameters with an amplitude modulation specified by the FSCS pattern. We will now omit the term A_{dp} to characterise the signature considering it as a scaling coefficient:

$$S_r^{\text{out}}(t) = A_{\text{tg}}(t)\sin\left[\frac{2\pi}{\lambda}\left(R_t(t) + R_r(t) - d\right)\right] \tag{13.39}$$

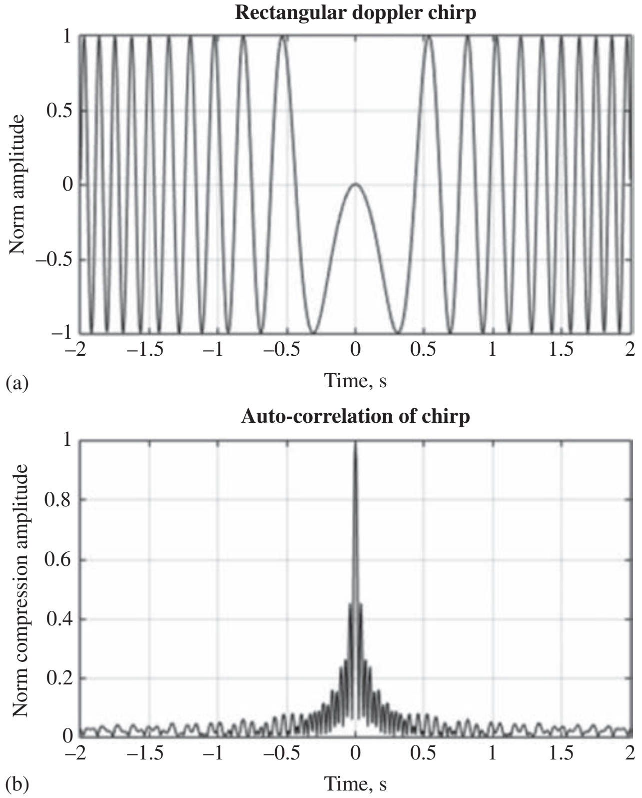

Figure 13.16 Example of a typical two-sided chirp forward scatter Doppler signature (with rectangular envelope) (a) and its auto-correlation function (b)

The actual signature envelope $A_{\mathrm{tg}}(t)$ is specified by the target FSCS and is unknown *a priori*. Even if the target and its trajectory are known, when modelling, analytical solutions for the FSCS are only available for a few convex shapes in the optical and sub-optical scattering regions [44–46]. Thus, approximated models from PO or PTD [45–47] or full-wave EM simulation methods [26] must be used for target FSCS estimation. However, the target still can be efficiently detected and its trajectory parameters estimated by means of the signal correlation with a matched phase Doppler signature where any amplitude modulation is omitted [10,28,41]. Then, the envelope of the target signature can be used for target automatic classification and imaging [6,23].

In [25], the nature of FSR target signature has been verified experimentally. A rectangular metal plate and identical plate covered with an absorber to avoid bistatic reflections were used as targets. The experimental results are shown in Figure 13.17(a), (b) and corresponding modelling in (c) using the rectangular aperture as described by (13.11) and extended for moving targets in [41].

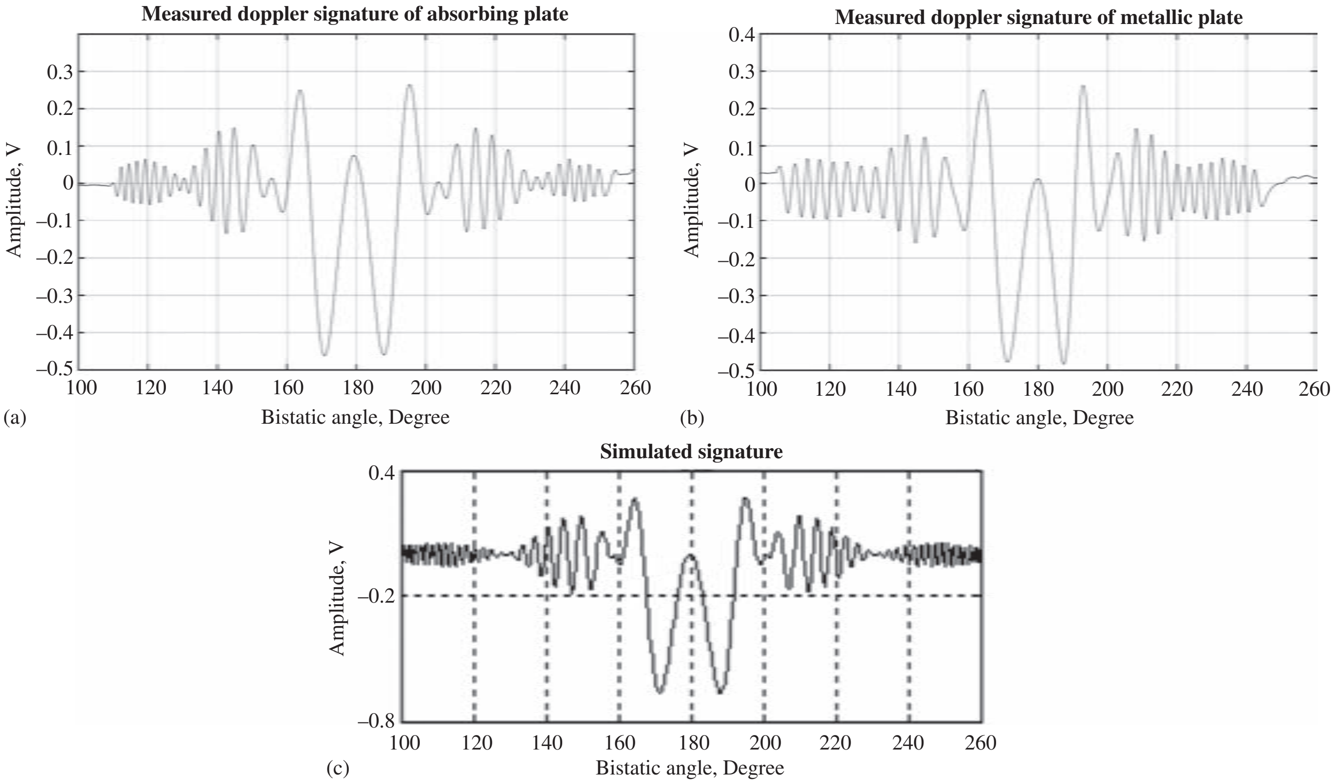

Figure 13.17 Comparison of the measured FS signatures of (a) absorbing plate (b) metal plate of the same size and (c) simulated signature [25]

Evidently, the envelopes and Doppler chirp carriers of measured and simulated signatures agree very well in the range of bistatic angles 140–220° that proves that the FS signature is correctly described by (13.39) as a product of Doppler carrier variation and the envelope specified by the FSCS. The amplitude in the middle part of the signal which lasts while the receiver is within the main shadow scatter lobe of the target does not depend on the material of the target but the size.

13.3.2.3 Examples of measured FSR signatures of real targets

Measured signatures of maritime targets in the upper C-band [25] with sizes defining different diffraction mechanisms are shown in Figure 13.18(a–c). Using the Fresnel parameter $S = D^2/(4\lambda)$, where D is the largest effective size of the target and λ is the wavelength, we will distinguish the Fraunhofer diffraction (far-field) region, $d \gg S$ and the Fresnel diffraction region, $d \sim S$, which define the scattering mechanism from the target in relation to the baseline distance d. However, when considering the time-varying Doppler signature of a moving target, we should not confuse diffraction from the individual target with the Fresnel-like diffraction on the effective inverse aperture defined by the whole path of the moving target which is 'seen' by the radar – as highlighted in Figure 13.19. Signatures were recorded at 7.5 GHz carrier and 300 m baseline. Figure 13.18(a) corresponds to a case of far-field diffraction from a small inflatable boat of size 2.9 m × 1 m (length and height above the surface), $S = 60$ m, where the DPS is essentially bigger than the shadow signal; signature of (b) corresponds to the case where the DPS is somehow comparable with the shadow signal and defines the boundary of the Fresnel to Fraunhofer diffraction zone for medium-size sailing yacht of 5 m length, $S = 160$ m; finally, (c) corresponds to the case of geometrical shadow where a large target essentially fully blocks the DPS, this is Fresnel diffraction from a large motor boat 15 m, $S = 630$ m. The most interesting case from a radar perspective

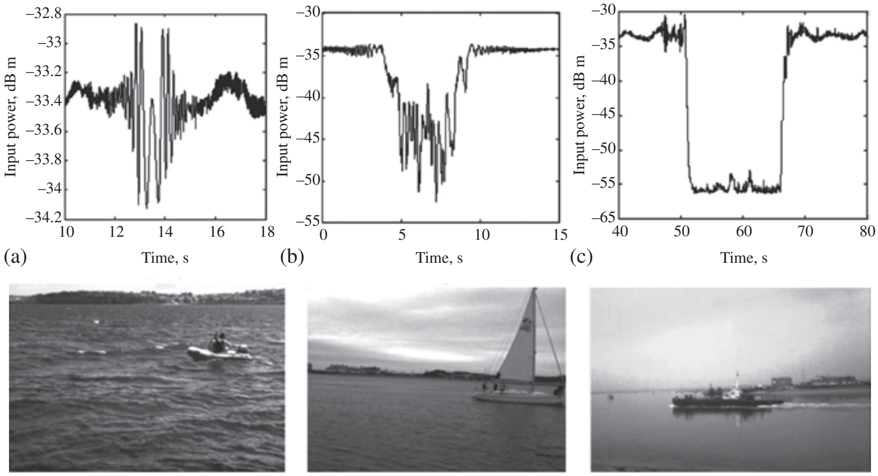

Figure 13.18 Recorded FS signature from targets crossing the middle of an FSR baseline of length d = 300 m [25]. (a) Small inflatable boat; (b) medium size yacht; (c) large motor boat

corresponds to (a) which may be considered as small target detection. In all signatures, the typical Fresnel diffraction behaviour (positive and negative contribution of phases of interfered signals) is visible, for cases (b) and (c) this is at the leading and trailing edges of the signature. Obviously, all three signals are liable to detection and, moreover, (b) and (c) are not difficult targets because their scattered signals are comparable with the LS. However, only the first signal is suitable for the extraction of target motion parameters as its waveform is fully defined by diffraction, describing the specific position and speed of the target passing through the constructive (in phase) and destructive (out of phase) zones over the path.

In Figure 13.20(a), the signature of an A321 aircraft of 44.5 m length crossing the 22 km baseline at 6 km from the receiver is shown for a passive version of FSR where a DVB-T signal of 650 MHz has been used [48]. In this case, S = 1,076 m; Figure 13.20(b) gives the signature of a 4×4 vehicle at 173 MHz and 100 m baseline, $S = 3.2$ m and (c), a human measured at a frequency ~64 MHz at 60 m baseline, $S = 0.2$ m. Thus, all the signatures obtained in the far field have clearly pronounced Doppler double-side chirp carriers with a unique envelope defined by the target silhouette.

Target classification is therefore possible by analysis of the signal envelope. Two approaches have been investigated so far. First is based on parametric analysis of the frequency domain waveform as reported in [49], where principal component analysis was used for automatic target classification. The second approach has been used for target shadow profile re-construction and requires knowledge of the complex envelope which can be extracted if two quadrature channels are used as discussed in [7,23,50].

13.3.3 Optimal signal processing in FSR

One of the objectives of optimal signal processing in FSR (as indeed in any radar) is to maximise SNR which is achieved by matched filtering. For some particular waveforms, signal waveform compression at the output of the matched filter is observed, where the auto-correlation function has a narrow main lobe with intensity

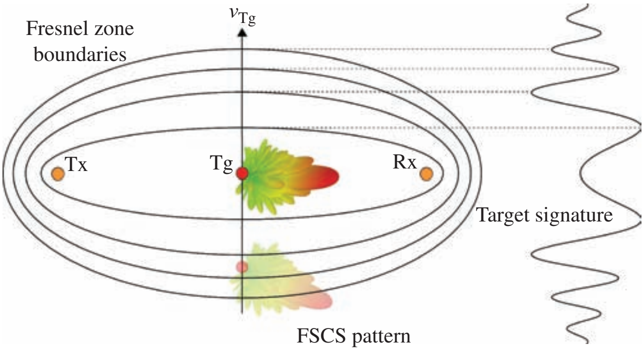

Figure 13.19 Target signature as composition of FSCS of the target forming the signal envelope and Doppler signature formed from passage of target through Fresnel zones

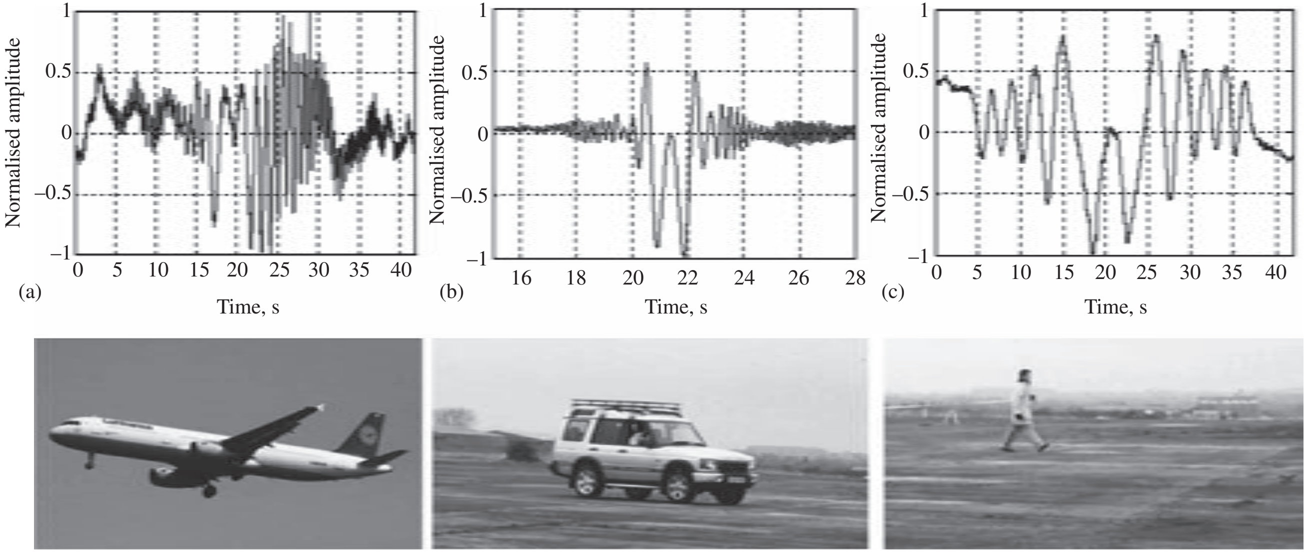

Figure 13.20 Recorded FSR Doppler signatures. (a) A321 aircraft using 650 MHz DVB-T signal (passive FSR), speed 400 km/h; (b) 4×4 vehicle at 173 MHz, middle crossing of 100 m baseline, speed 32 km/h (c) human being at 64 MHz, middle crossing of 60 m baseline, 6 km/h

much greater than that of the sidelobes. As shown before (Section 13.3.2.1), in FSR, the received Doppler waveform is a double-sided chirp signal which after matched filtering will demonstrate such a compression [20].

The SNR improvement achieved by matched filtering can be characterised by the signal processing gain G_{SP}. Considering the fundamental case of the target crossing, the baseline at the midpoint, its visibility time will be given by, $T_{\max} = \left(d/v_{tg}\right)\tan\alpha$, where α is the maximal diffraction (excursion) angle of the target from the receiver, and the maximal Doppler deviation during this time will be:

$$f_d^{\max} = 2f_c\frac{v_{tg}}{c}\sin\alpha \tag{13.40}$$

Thus, the signal processing gain/time bandwidth product can then be estimated as:

$$G_{sp} = T_{\max}\cdot 2f_d^{\max} = 4d\frac{f_c}{c}\tan(\alpha)\cdot\sin(\alpha) = 4d\frac{1}{\lambda}\tan(\alpha)\cdot\sin(\alpha) \tag{13.41}$$

where f_c is the carrier frequency, v_{Tg} is the target speed normal to the baseline, c is the speed of light. Using the -3 dB level of the FS main lobe as the reference, this angle can be approximated according to (13.5) as $\alpha \approx (\lambda/2l_{\text{eff}})$ giving,

$$G_{sp} = 4d\frac{1}{\lambda}\tan\left(\frac{\lambda}{2l_{\text{eff}}}\right)\cdot\sin\left(\frac{\lambda}{2l_{\text{eff}}}\right) \tag{13.42}$$

where l_{eff} is the effective target length. It is important to notice that the gain does not depend on v_{tg} due to the inverse dependence of the Doppler variation and observation time with regard to the target speed. It can also be seen that for targets of larger length, for a given frequency, the processing gain is reduced due to the effect of the narrowing FS main lobe width, which works to reduce both the maximal Doppler and the integration time under consideration. Indeed for small angles α, (13.42) can be approximated further by:

$$G_{sp} \approx d\frac{\lambda}{{l_{\text{eff}}}^2} \tag{13.43}$$

In summary, the processing gain in FSR offers advantages in the detection of the smaller targets (in length) where it is potentially most required, and less so in the case of the larger length targets which will assumedly have larger maximal FSCS, thus the need for as high a processing gain is in any case reduced. Actual estimations of processing gain for different targets, carrier frequencies and baseline lengths are presented in [41].

13.3.3.1 Target motion parameter estimation

Due to the lack of range resolution in FSR (particularly in the case of continuous wave (CW) signals), target motion/trajectory parameters have to be inferred via other means. This is the other very important output of the matched filter, the ability to extract the target motion parameters as indeed these are the inputs to the matched filtering process and design of matched waveforms. In accordance with the optimal detection theory [51 (Ch.7)], the maximal SNR in the presence of additive white Gaussian noise can be obtained by correlation of the received signal $S_r(t)$ with a reference function $S_{\text{ref}}(t)$, where the reference function is an exact but conjugated copy of the actual target signature for a given target type and trajectory, as given by:

$$S_{\text{opt}}(\tau) = \int_{-T/2}^{T/2} S_r(t) S_{\text{ref}}(t-\tau) dt, \quad S_{\text{ref}}(t) = S_r^*(t) \tag{13.44}$$

where T is the integration time duration equal to the target visibility time as in Section 13.2.2.1. Thus, the optimal filtering process in FSR represents the problem of sequential correlation of the received signal with a set of pre-defined reference waveforms corresponding to the expected target types and motions. The task is to define a set of reference functions for the correlation. As shown in Section 13.3.2.2, the target signature can be described by (13.39), and this therefore is the generalised form of the reference waveform for the matched filtering, $S_{\text{ref}}(t)$. The received signal in FSR depends on the target's speed, trajectory and FSCS which are all unknown *a priori* and in turn define the parameters $R_t(t)$, $R_r(t)$ and $A_{\text{tg}}(t)$ in the equation. Strictly speaking, all these parameters should be estimated when producing the reference waveforms and for a given range of expected velocities and trajectories both $R_t(t)$ and $R_r(t)$, which define the phase signature, can be modelled effectively. However, there is difficulty in describing the amplitude/envelope parameter $A_{\text{tg}}(t)$, which refer to a particular targets FSCS pattern (with small contribution from propagation factors). Thus, reference waveforms would need to be created for not only each set of expected motion parameters, but all possible expected target shapes and sizes as well.

It turns out however that complete knowledge of the signal envelope is not necessary for effective signal compression. The major correlation properties between fast sign alternating functions are mainly specified by their sign functions rather than their amplitude variation; thus, the more slowly varying envelope function $A_{\text{tg}}(t)$ is actually equivalent to a window function which only serves to weight the compression output. This effect has been highlighted by example in [26] and is reproduced in Figure 13.21.

Figure 13.21(a) shows an FSR chirp signal with rectangular, actual FSCS and Kaiser (shape factor 2.5) envelopes. Figure 13.21(b) gives the normalised cross-correlations of the FSCS-windowed chirp with itself (auto-correlation) and with the other two signals. It is noted that even when cross-correlating with the rectangular chirp (no envelope variation), the correlation coefficient only reduces to 0.88. On the other hand, Figure 13.21(c) shows two chirps which differ in instantaneous frequency by 10% and (d) shows the dramatic effect this phase difference has on the correlation coefficient. Thus, the inaccuracy in phase has a much more detrimental effect on the correlation coefficient compared to that of the envelope.

Thus, the reference waveforms for matched filtering, $S_{i,j,k}$ are defined to replicate the phase signature accurately to cover a desired range of velocities and trajectories where *i, j* are indices of velocity components $\left(v_{x,i}, v_{y,j}\right)\big|_{i=1..Nx, j=1..Ny}$ and k is the index of baseline crossing points $\left(y_{c,k}\right)\big|_{k=1..K}$. Analysis of the selection of velocity increments can be found in [41]. The approximation of the envelope parameter leads to the

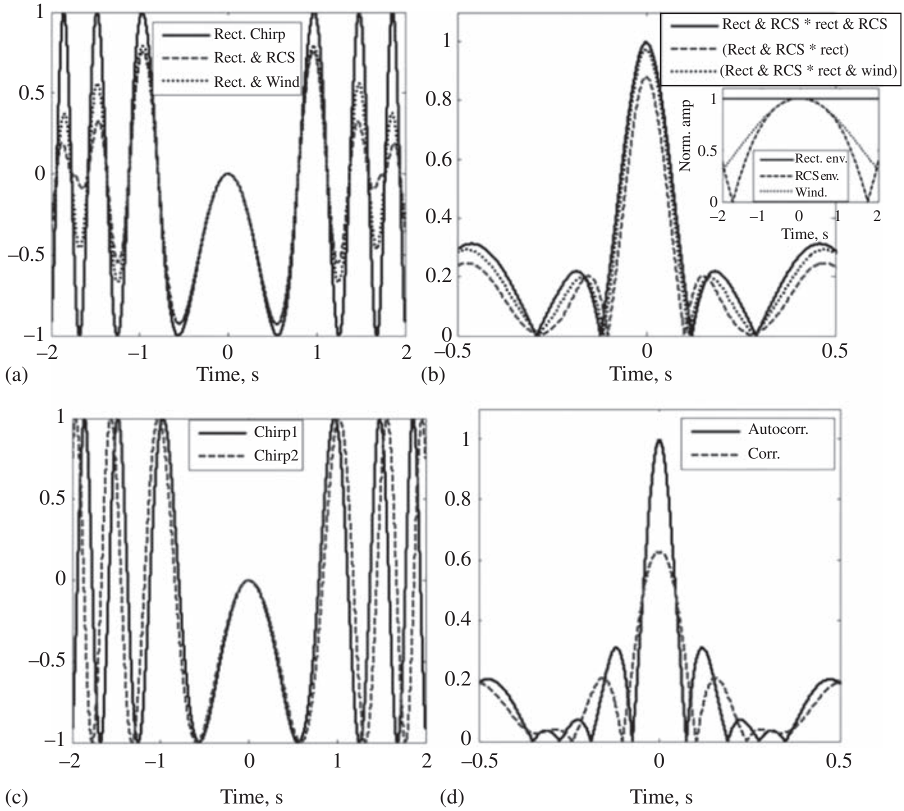

Figure 13.21 Effect of envelope and phase on waveform correlation outputs [25]. (a) shows chirp signals with rectangular, FSCS and Kaiser windowing, (b) gives the normalised correlation outputs of each chirp with the FSCS-windowed chirp. Two chirps differing in frequency by 10% are shown in (c) with the corresponding normalised correlation and cross-correlation outputs in (d)

re-phrasing of this processing to being referred to as quasi-optimal rather than optimal due to the slight processing loss related to the amplitude mis-matches. Figure 13.22 shows the simplified block diagram of such correlation processing, where subscript *m* indicates the ‘matched’ signal/parameters and previously undefined HPF and BPF represent high and band pass filters respectively.

The matching waveform delivers a global maximum of all of the correlations, and from this the trajectory and speed are found. Information regarding the shape/size of the target can then be found using profile re-construction algorithms [24]. To provide an example of the output of such processing, Figure 13.23(a–c) show the results of processing of recorded maritime signatures for the same target, a 2.9 m long inflatable boat, but with varying trajectories and baselines [25].

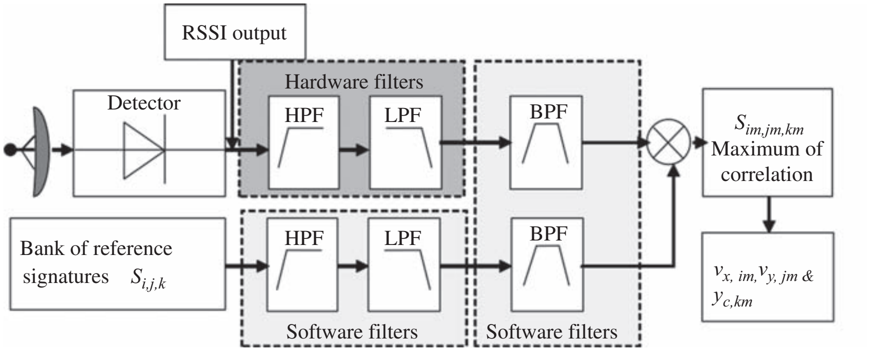

Figure 13.22 Flow chart of matching filtering procedure [25]

Table 13.5 shows the extracted motion parameters (parameters used to form the best matching reference function), along with global positioning system (GPS) tracked values. Crossing points refer to the crossing distance from the baseline centre.

It can be seen, when considering Figure 13.23 and Table 13.5, even in cases when the true signal envelope appears very dissimilar to the reference, good estimations of the target motion parameters can be obtained purely by the Doppler phase matching.

13.3.3.2 Convoy resolution

Another advantage of the optimal signal processing is the improved ability to resolve targets in convoy. The compressed signal has a duration of ΔT that is approximated by the inverse of the bandwidth of the original received signal. So in FSR, relating to the maximal expected Doppler, $f_d^{\max}$, as in (13.40),

$$\Delta T \approx \frac{1}{2f_d^{\max}} \approx \frac{\lambda}{4v_{\text{tg}} \sin \alpha} \tag{13.45}$$

where α is defined in (13.42) and can be approximated for the -3 dB FSCS main lobe width to give:

$$\Delta T \approx \frac{\lambda}{4v_{\text{tg}} \sin(\lambda/2l_{\text{eff}})} \tag{13.46}$$

and could be further simplified in the case of electrically large targets (small main lobe widths). In addition to effect of bandwidth on compressed width, the processing gain itself (and thus integration time) still needs to be large enough to reduce the compression sidelobes to satisfactory levels.

As an example of compression, results are shown in Figure 13.24 for measured signals at 64 and 434 MHz of two humans walking at 6 km/hr separated by 5 m with a baseline of 100 m. The increase in carrier frequency and thus resolution improvement facilitates the ability to separate the two targets; as seen in the 434 MHz results compared to the 64 MHz case.

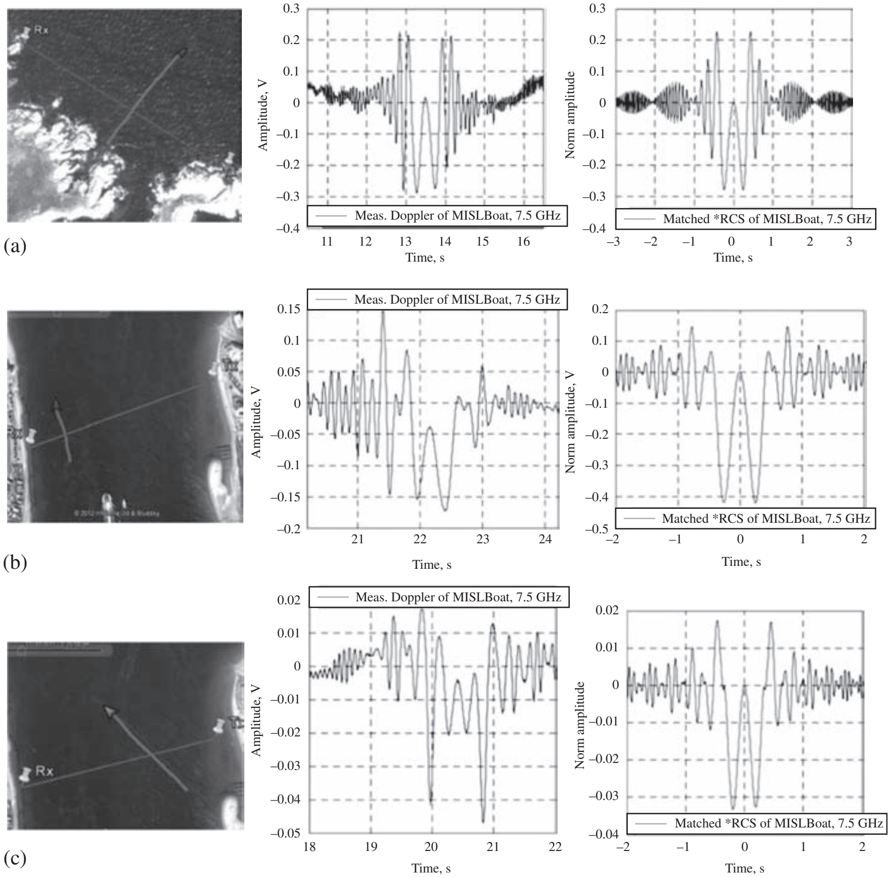

Figure 13.23 Example of measured maritime target signatures and matched waveforms from correlation processing [25]. Left panels shows target trajectory, middle panels are measured signatures, right panels are matched waveforms

Table 13.5 Extracted motion parameters for example target signatures shown in Figure 13.23 [25]

Figure 13.23	Baseline (m)		Speed (km/h)	Crossing angle (°)	Crossing point (m)
(a)	350	GPS	18.5–19.1	~90	12
		Extracted	19.08	90.0	20.0
(b)	285	GPS	12.2–13.0	~90	85.5
		Extracted	13.	90.0	80.0
(c)	262	GPS	16.7–19.1	~60	40
		Extracted	17.64	60.0	60.0

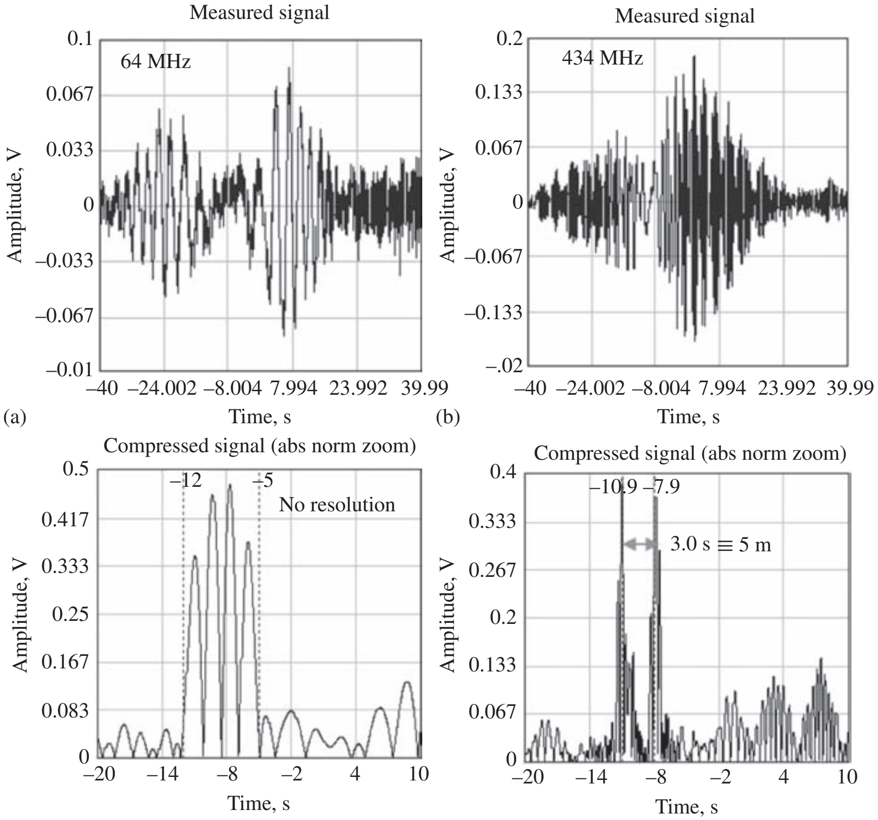

Figure 13.24 Experimentally measured signals of two human targets in convoy and their corresponding compressed signals at two frequencies: (a) 64 MHz and (b) 434 MHz

13.4 Clutter in FSR

Clutter in FSR is related to a dynamic change of the underlying surface and the surrounding environment, which in the case of ground-based FSR is mainly associated with vegetation and for maritime FSR it is the dynamic sea surface. Unlike the monostatic case, where directional antennas and the presence of range resolution lead to clutter being collected from only a limited area, or even in the case of FSR intended for airborne target detection, surface-based target detection in FSR is to be performed in the background of strong Doppler modulated clutter. This clutter is collected from a large volume around and between the transmitter and receiver, where spatially distributed clutter sources will cause backscatter, bistatic and FS signal interference. The main clutter-related problems are associated with: (i) target detection if the spectrum of Doppler modulated clutter overlaps with the target return spectrum; (ii) general non-Gaussian behaviour where long tails of the clutter intensity distribution results in an increased false alarm rate.

Statistical and spectral characteristics of FSR clutter need to be distinguished and studied separately in three main applications of FSR: ground-based target detection, seaborne target detection and airborne target detection, the last being the least affected by clutter. We will therefore give a brief overview of spectral and statistical properties of clutter related to first two cases.

13.4.1 Vegetation clutter

In a ground sensor network, the variations in the generic received signal caused by surrounding wind-blown vegetation may be attributed to one of following mechanisms: multi-path interference, de-polarisation, signal attenuation due to absorption and scattering [52]. As a result, at the reception side, the dominant component of the received signal is accompanied by the time-variant component, which introduces the fading of the received signal. Doppler modulation (magnitude and waveform) caused by this component depends on the wind strength.

In such a context, FSR clutter may be investigated using the statistical approaches used for characterisation of RF channels in communications [53], where wind strength is introduced as an additional parameter. In communication systems theory, fading of the RF channel over forested paths are widely reported and the interested reader can find as such in, for instance, [54–56].

A long-term experimental study has been undertaken in the ultra-high/very high frequency (UHF/VHF) bands, at different sites with terrain profiles varying from a concrete runway to dense woodland during different seasons as reported in [53,57]. The PSD of clutter signals for each operational frequency channel, time variation of average clutter power, dependence of clutter power on baseline range, frequency, wind speed and direction and probability density function (PDF) of clutter amplitudes have been estimated. A few peculiarities in comparison to monostatic clutter have been found in relation to the PSD and to statistical distribution:

Power and power spectrum. The power spectrum width is limited by 1–2 Hz invariantly on carrier frequency; PSD decreases by 40 dB per decade of Doppler frequency, while the total power magnitude increases with the carrier frequency by fourth power as in Figure 13.25. By comparison with wind records, it has been concluded that the wind strength determines the clutter power variations which are non-stationary in the general case.

Statistical properties. Wind strength affects the PDF of the clutter intensity amplitude: for low wind, it is close to Rayleigh, or Weibull distribution with the shape factor of 2, and therefore, the Weibull distribution have been used as a reference. The higher the wind power and the carrier frequency, the smaller is the shape factor. In addition, PDF's of recorded clutter deviate more from the Weibull fit, demonstrating an increase of the 'tail' in the distribution. This indicates potentially worse radar performance in terms of probability of false alarms.

Clutter modelling. A semi-deterministic approach to model clutter has been suggested in [27,57], where clutter has been presented as a sum of scattered signals

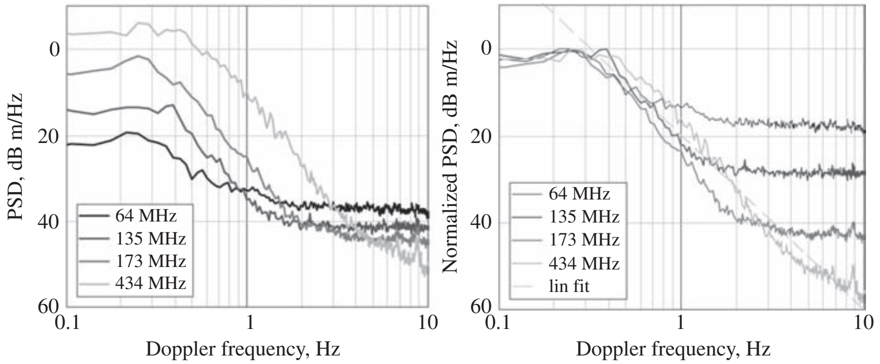

Figure 13.25 Power spectrum density of vegetation clutter in FSR measured at different frequencies (left – absolute values, right – normalised to maximum) – © [2010] IEEE. Reprinted, with permission, from [57]

from elementary oscillators associated with leaves, branches and the trunk of a tree. The statistical behaviour of the oscillators was imitated by randomly distributed initial phases, their location points around a single centre and their amplitudes distributed within a range appropriate for the tree parts. It has been shown that spectral characteristics of the modelled clutter mentioned above are in excellent agreement with results of measurement. Moreover, the statistical distribution has also been in agreement with that of experimentally observed signal and a simulation model of the clutter signal has been developed to be used in a synthetic simulation environment to test FSR radar performance.

13.4.2 Sea clutter

FSR for maritime application, proposed in [5,58] and investigated in [26,39,59,60], is configured as a fence consisting of nodes separated by distances of the order of a kilometre. To form such a fence, the node transceivers are mounted on buoys and therefore low grazing angle with respect to the sea surface is expected. The effect of the sea is 2-fold, (i) it forms an underlying surface as in the TRP propagation model and (ii) complex scattering on the spatially distributed dynamic sea waves is responsible for a sea clutter which will be received from a large illuminated area between buoys.

By its very configuration, the FSR channel is similar to an RF communication channel, and therefore, sea clutter can be described in terms of fading in an RF channel over a sea surface. Forward propagation studies over the sea surface have been dedicated to characterise radio wave propagation [61–68], coastal or ship-to-ship communications [35,63,69–72] as well as radar scattering at low grazing angles in [64–68,70,73,74]. In [17], approaches developed for characterisation of fading of RF channels were applied for analysis of FSR clutter at very low grazing angle. Both spectral and statistic properties were measured and analysed, and results were compared to results of modelling. In particular, the dependence of scattering mechanisms – dominant specular reflections, diffused scattering and partial shadowing – on the sea state has been considered. In summary;

- forward-scatter radar sea clutter measured at very low grazing angles (less than 0.5°) exhibits, to a first approximation, a near constant frequency centred below 1 Hz, with a roll off of approximately 35–40 dB per decade in the Doppler frequency domain – Figure 13.26(a). It has also been shown that Rayleigh is a good fit to the measured clutter intensity distribution – Figure 13.26(b) and (c);
- the clutter spectrum and shape of distribution function are found to be independent of transmit receive/baseline range, sea state and carrier frequency, within the range of limited experimental conditions.

13.5 Air target tracking in CW FSR

This section is dedicated to target tracking in FSR via the maximum likelihood method. The main goal is to obtain the accuracy of maximum likelihood estimations of target co-ordinates. This accuracy is calculated theoretically and mathematical modelling results are also presented.

13.5.1 Target resolution in forward scatter radar

The advantages of using the FS configuration of bistatic radar when detecting low-observable targets, including targets built with stealth technology are described in the previous sections of this chapter. Technical solutions applied when developing FSR for detection and tracking of air targets are based on the principles discussed above, but require some specific clarifications.

One of the main characteristics of any radar is target resolution. For the radars with a pulse probing signal, range resolution is inversely proportional to the signal bandwidth. At the same time, in bistatic radar, to provide range resolution, we should resolve the target scattered signal from the direct transmitter signal. A very particular feature of FS configuration is strong stretching of the coverage along the baseline [15 (p.400), 75]. Thus, the time delay of the scattered signal with respect to direct signal is very small. Simple geometrical calculations show that to provide range resolution of about 100 m with a baseline length of about 40 km, we should use a pulse-probing signal with a band width of more than 100 MHz [15 (p.403)].

Realisation of the transmit and receive positions providing formation and processing of a signal with such bandwidth is both a difficult and expensive solution. FSR with narrowband CW probing signal (quasi-harmonic signal) provides Doppler resolution simultaneously with the possibility of long enough (theoretically, during the whole observation time) coherent signal integration. For an integration time of 1 s, we have Doppler resolution of 1 Hz and the Doppler shifts of the signals scattered by two targets moving with the same velocity but placed at different points inside of the FSR coverage are different [15 (p.403)]. Therefore,

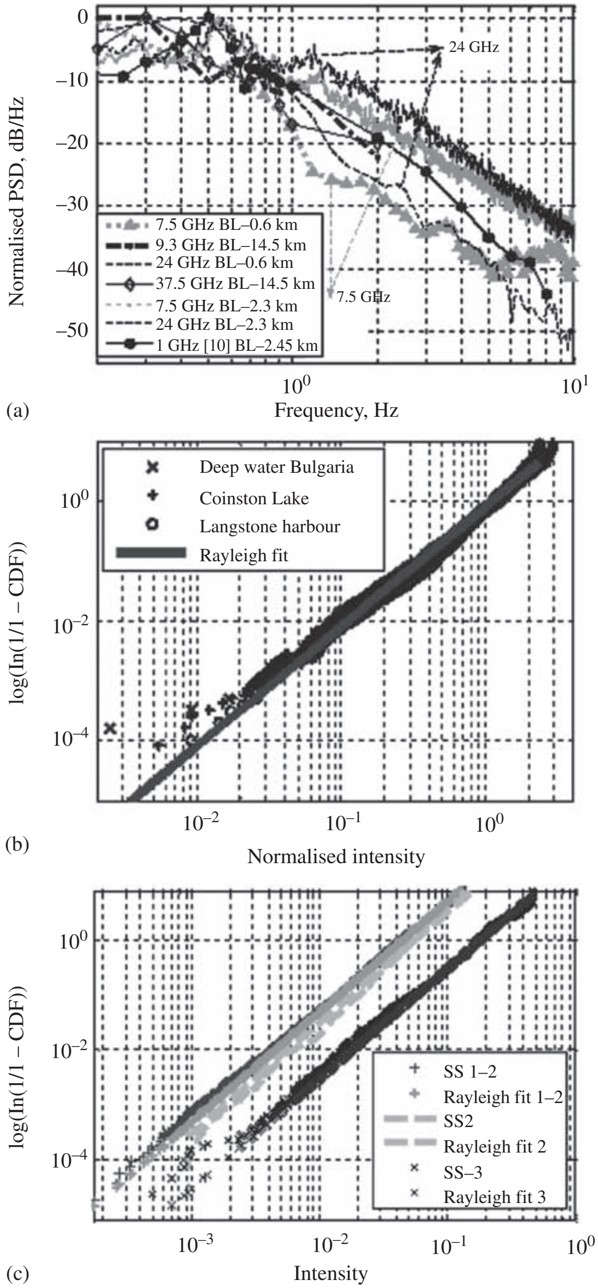

Figure 13.26 *(a) Normalised PSDs of FSR sea clutter recorded at varying frequencies, ranges, sea states and test sites. (b) Cumulative distribution function (CDF) of normalised FSR sea clutter from different test sites on Weibull paper and (c) comparison of CDFs for long-term FSR sea clutter measurements in different sea states. SS stands for sea state by Douglas scale (plots collated from [17])*

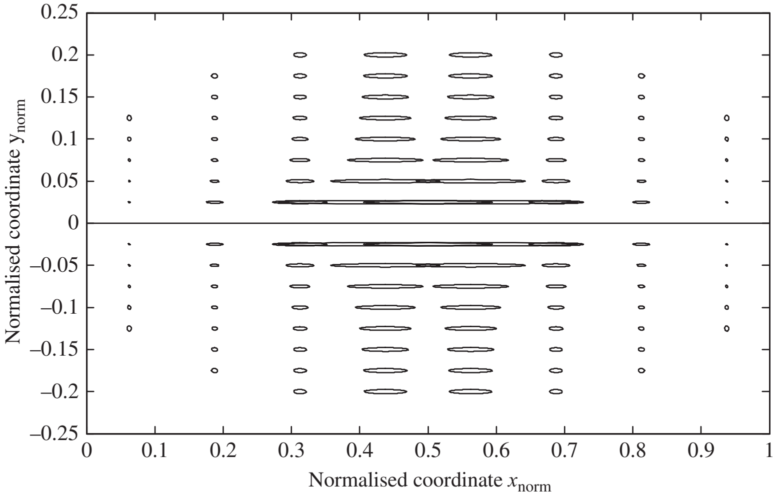

Figure 13.27 Resolution ellipses vs normalised co-ordinates

Doppler resolution in FSR during the tracking of moving targets provides spatial resolution. Simple calculations obtained with the equations concatenating the values of Doppler shift with the target Cartesian co-ordinates [15 (p.412), 76,77] show that in FSR, with the length of baseline equal to 40 km, wavelength of probing signal equal to 0.2 m and integration time of 1 s, we have spatial resolution along the baseline of about 200 m and approximately 20 m across the baseline.

In Figure 13.27, the spatial resolution of CW FSR is presented in the form of ellipses. The axes of these ellipses are equal to the resolution along the x and y co-ordinates. The captures along x and y axes are normalised to the length of the baseline and the ellipses with the smaller axes correspond to the areas where the better resolution is provided. It is seen that the best resolution corresponds to the areas close to transmit and receive positions ($x_{norm} = 0$ or 1, $y_{norm} = 0$), the worst is observed in the middle of the baseline.

Thus, we can make the conclusion that a narrowband CW-probing signal is an optimal solution for ground-based FSR aimed at tracking airborne targets, due to the low cost, simple implementation, low transmitted power and target resolution in Doppler domain equal to the appropriate spatial resolution.

13.5.2 FSCS and coverage when tracking air target

FSR should be able not only to detect targets crossing the baseline but also provide tracking of these targets. The best way to understand the possibilities of air target detection and tracking in FSR is to consider some results of FSCS calculation for a typical air target, together with the experimental results of tracking.

In Figure 13.28, an example of calculation of the azimuth plane FSCS for a helicopter is shown for two wavelengths of 0.3 m and 1 m (curves 1 and 2,

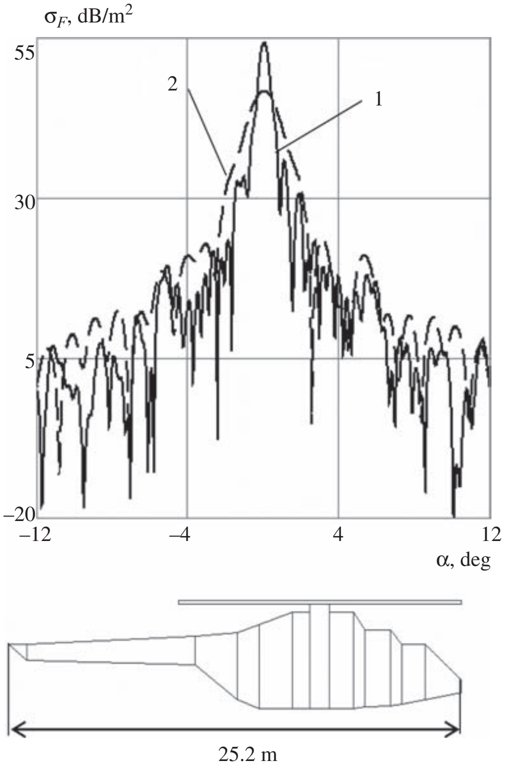

Figure 13.28 An example of helicopter azimuth plane FSCS at two different wavelengths of 0.3 m and 1 m (curves 1 and 2, respectively) – © [2007] John Wiley and Sons. Reprinted, with permission, from [15]

respectively). As it is seen, the width of the main lobe of FSCS is only about 1°. At the same time, the value of the FSCS is large (more than the monostatic RCS which is equal to about 2 m^2) up to values of target azimuth exceeding 10°. Thus, the region, where FSCS is bigger than the monostatic RCS, is much wider than the width of the main lobe.

Experimental results of detection and tracking of the same target are shown in Figure 13.29. The grey region presents FSR coverage for the helicopter calculated via the radar equation for the bistatic system. When calculating this coverage, the helicopter FSCS shown in Figure 13.28 was used. The indices from 1 to 5 are the numbers of the target tracks obtained during the experiment. It is easily seen from Figure 13.29 that target was detected and tracked for values of azimuth of more than 10°. Therefore, detection and tracking of air targets in CW FSR is provided in the region of several sidelobes of the FSCS as well as in the region of the main lobe.

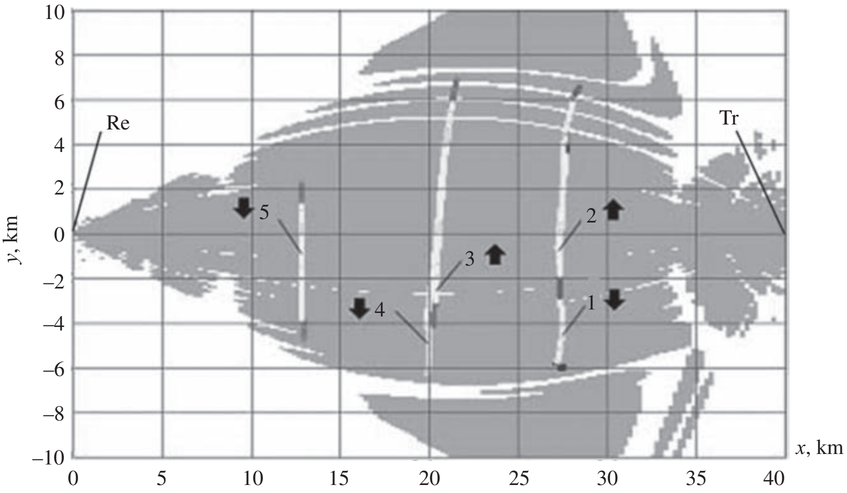

Figure 13.29 Example of target tracking inside of the coverage – © [2007] John Wiley and Sons. Reprinted, with permission, from [15]

13.5.3 Mathematical model of measuring process. Maximum likelihood estimation of trajectory parameters

The three-dimensional bistatic FSR geometry is shown in Figure 13.30. In Figure 13.30, Tr is the transmitting position; Re the receiving position; Tg is the target; AB is the target trajectory; CD is the projection of the target trajectory onto the horizontal plane; x, y, z represent the orthogonal co-ordinate system attached to the receive position; x_0 is the x co-ordinate of the baseline crossing projection; φ is the target trajectory inclination angle towards the baseline in the horizontal plane; ψ is the angle of the target trajectory inclination in the vertical plane; α is the current target azimuth; β is the current target angle of elevation; $\tilde{\beta}_B$ is the bistatic angle.

We will consider three-dimensional bistatic FSR providing estimation of three target Cartesian co-ordinates (x, y, z) and the three components of the target velocity vector (v_x, v_y, v_z). When using a narrowband CW-probing signal, the primary parameters to be measured are the angles of arrival of the target scattered signal (azimuth, α_i and elevation angle, β_i) and Doppler frequency shift $f_{D,i}$ [15 (p.417)], [77–80], where i labels the time instance corresponding to the ith measurement.

When the length of the baseline is equal to several tens of kilometres, the airborne target is usually observed during the time interval of one to several minutes. Each measurement of primary parameters is obtained after target return coherent integration and detection during a time interval which is short enough to neglect the variation of Doppler shift. General techniques to provide measurement

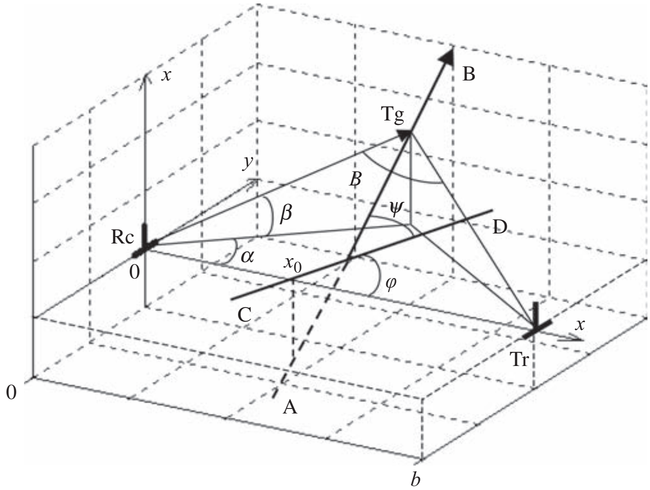

Figure 13.30 Three-dimensional bistatic forward scattering radar geometry – © [2007] John Wiley and Sons. Reprinted, with permission, from [15]

of these parameters are described in [15 (p.417), 81]. When observing typical airborne targets (aircraft, helicopter), the interval of signal integration does not exceed 1 s, the base of scattered signal, B, is close to unity [15 (p.418), 82]. Measurement of Doppler shift could be provided via standard methods of digital spectral analysis (fast Fourier Transform). Measurements of angles could be obtained via monopulse techniques when forming partial beams of the directivity pattern of the antenna in azimuth and elevation planes [15 (p.419)]. To provide angular measurements, an antenna array is used at the receiver.

The sequence of primary measurements forms a vector:

$$\mathbf{z}_n = \left[\hat{f}_{D1}, \hat{\alpha}_1, \hat{\beta}_1, \hat{f}_{D2}, \hat{\alpha}_2, \hat{\beta}_2, \ldots \hat{f}_{Dn}, \hat{\alpha}_n, \hat{\beta}_n\right]^T \tag{13.47}$$

Since the coverage of FSR is narrow enough, the probability of target manoeuvre inside this coverage is small. Therefore, a model of linear motion is the most appropriate. For the case when the trajectory model is assumed to be linear, the tracking vector is written as follows:

$$\mathbf{x}_n = \left[x_n, y_n, z_n, v_x, v_y, v_z\right]^T \tag{13.48}$$

where x_n, y_n, z_n, v_x, v_y, v_z are the values of target Cartesian co-ordinates and their derivatives at observation moment, t_n.

A non-linear system of equations concatenating the values of primary parameters with the values of trajectory parameters appears as follows [15 (p.412)]:

$$
\begin{aligned}
f_{Di}(\mathbf{x}_n) &= -\frac{1}{\lambda}\left\{
\begin{array}{l}
\dfrac{[x_n - v_x(n-i)T]v_x + [y_n - v_y(n-i)T]v_y + [z_n - v_z(n-i)T]v_z}{\sqrt{[x_n - v_x(n-i)T]^2 + [y_n - v_y(n-i)T]^2 + [z_n - v_z(n-i)T]^2}} \\
+\dfrac{[y_n - v_y(n-i)T]v_y - [b - [x_n - v_x(n-i)T]]v_x + [z_n - v_z(n-i)T]v_z}{\sqrt{[b - [x_n - v_x(n-i)T]]^2 + [y_n - v_y(n-i)T]^2 + [z_n - v_z(n-i)T]^2}}
\end{array}
\right\} \\
\alpha_i(\mathbf{x}_n) &= \operatorname{arctg}\frac{y_n - v_y(n-i)T}{x_n - v_x(n-i)T} \\
\beta_i(\mathbf{x}_n) &= \operatorname{arctg}\frac{z_n - v_z(n-i)T}{\sqrt{[x_n - v_x(n-i)T]^2 + [y_n - v_y(n-i)T]^2}}
\end{aligned}
\tag{13.49}
$$

A model of the measuring process is based on (13.49). Statistical dependence of the measured values of the primary parameters upon the target trajectory parameters is described by a measurement equation. It can be written in the following compact form [15 (p.421), 77]:

$$\mathbf{z} = \mathbf{h}_n(\mathbf{x}_n) + \Delta\mathbf{z}_n \tag{13.50}$$

$$
\begin{aligned}
\mathbf{h}_n(\mathbf{x}_n) = [&f_{D1}(\mathbf{x}_n), \alpha_1(\mathbf{x}_n), \beta_1(\mathbf{x}_n), f_{D2}(\mathbf{x}_n), \alpha_2(\mathbf{x}_n), \beta_2(\mathbf{x}_n), \ldots \\
&f_{Di}(\mathbf{x}_n), \alpha_i(\mathbf{x}_n), \beta_i(\mathbf{x}_n), \ldots, f_{Dn}(\mathbf{x}_n), \alpha_n(\mathbf{x}_n), \beta_n(\mathbf{x}_n)]^{\mathrm{T}}
\end{aligned}
\tag{13.51}
$$

where $\mathbf{h}_n(\mathbf{x}_n)$ is a non-linear vector function with elements defined by (13.49); $\Delta\mathbf{z}_n$ is a vector of random primary measurement errors.

For further consideration, we suppose that primary measurement errors are Gaussian with zero mean and variances, $\sigma_f^2, \sigma_\alpha^2, \sigma_\beta^2$, which are considered to be the same for all instances in time. We also suppose that the measurements of the primary parameters are mutually independent at any time shift, as well as the measurements of every parameter being independent at different moments of observation.

Using the accepted Gaussian model of primary measurement errors, the maximum likelihood estimation of the tracking vector, $\hat{\vec{x}}_n$, can be found as:

$$\hat{\mathbf{x}}_n = \arg\min \varphi_n(\mathbf{x}_n) \tag{13.52}$$

where $\phi_n(\mathbf{x}_n) = [\mathbf{z}_n - \mathbf{h}(\mathbf{x}_n)]^T \mathbf{G}_n [\mathbf{z}_n - \mathbf{h}(\mathbf{x}_n)]$; $\mathbf{G}_n = \left[M\left\{\Delta\mathbf{z}_n \Delta\mathbf{z}_n^T\right\}\right]^{-1}$ is an inverse correlation matrix of the primary measurement error vector, $\Delta\vec{z}_n$.

13.5.4 Potential accuracy of trajectory parameters measurement

When using the maximum likelihood method, the potential accuracy is determined by the Fisher information matrix. For the observation process of the introduced model of the measuring process, the elements of the Fisher matrix of [79,83 (p.325)] are defined as:

$$\mathbf{J}_{lk}(\mathbf{x}_n) = \frac{1}{\sigma_f^2}\sum_{i=1}^{n}\left[\frac{\partial f_{Di}(\mathbf{x}_n)}{\partial x_l}\cdot\frac{\partial f_{Di}(\mathbf{x}_n)}{\partial x_k}\right] + \frac{1}{\sigma_\alpha^2}\sum_{i=1}^{n}\left[\frac{\partial \alpha_i(\mathbf{x}_n)}{\partial x_l}\cdot\frac{\partial \alpha_i(\mathbf{x}_n)}{\partial x_k}\right] + \frac{1}{\sigma_\beta^2}\sum_{i=1}^{n}\left[\frac{\partial \beta_i(\mathbf{x}_n)}{\partial x_l}\cdot\frac{\partial \beta_i(\mathbf{x}_n)}{\partial x_k}\right] \tag{13.53}$$

where x_l, x_k are elements of the vector $\mathbf{x}_n$ ($l, k \in [1,6]$ ($x_1 = x_n$, $x_2 = y_n$, $x_3 = z_n$, $x_4 = v_x$, $x_5 = v_y$, $x_6 = v_z$).

Variances $\sigma^2_{x,n}$, $\sigma^2_{y,n}$, $\sigma^2_{z,n}$, $\sigma^2_{vx,n}$, $\sigma^2_{vy,n}$, $\sigma^2_{vz,n}$ of the estimates of trajectory parameters can be calculated as diagonal elements of a matrix inverse to the Fisher matrix. In Figure 13.31, dependences of the normalised root-mean-square deviations of the estimates of co-ordinate x as functions of value of co-ordinate y are shown by curves 1 and 2. These are calculated for $\sigma_f = 1$ Hz; $\sigma_\alpha = 0.5°$ for two different target trajectories with parameters $\varkappa_{CR}/b = 0.75$; $\varphi = 45°$ (Figure 13.31(a)) and $\varkappa_{CR}/b = 0.25$;,$\varphi = 45°$ (Figure 13.31(b)). Curve 1 corresponds to an altitude of 2 km, while curve 2 is calculated for zero altitude. It was assumed that $b = 40$ km, $V = 200$ m/s, $\lambda = 1$ m, $T = 0.25$ s.

The analysis of the plots shows that practically monotonic reduction of rms deviations of errors of co-ordinate x estimation takes place while the observation time increases (at small values of the angle α they practically coincide with rms deviations of target range estimation errors), but insignificant rise near the baseline is possible. The degradation in accuracy of the estimation of co-ordinate x at the moment of crossing the baseline can be explained by the fact that the Doppler frequency shift on the baseline does not depend on x. The large errors at the initial segment of the trajectory can be explained by the lack of measurements of the

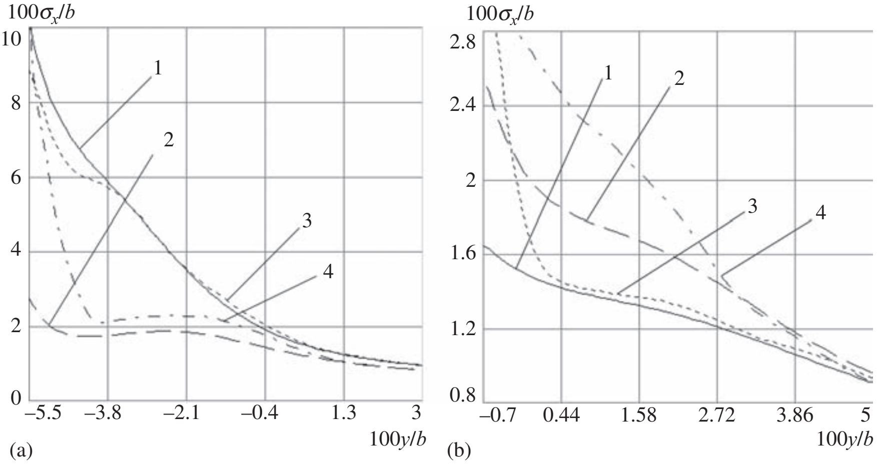

Figure 13.31 Rms errors of target tracking

primary parameters. At the moment the target leaves the coverage, the rms deviation of the error of estimation of co-ordinate x becomes sufficiently small, about 0.5%–1% of the length of the baseline under the conditions described above. From comparison of the results presented in Figure 13.31(a) and (b), we can see that the behaviour of the tracking accuracy in relation to target altitude is different when the target moves closer to the transmit position, Figure 13.31(a), and closer to receive position, Figure 13.31(b). In the first case, the accuracy is worse when the altitude is bigger, while in the second case the inverse situation takes place. There are two reasons for this: first, the rate of change of primary parameters depends on the target location between the transmit and receive sides. This is higher when the target is near to the receiver; second, when target altitude is not equal to zero, the measurements of elevation angle become more informative. This is equivalent to the increasing of the length of the primary measurement vector, $\mathbf{z}_n$, in comparison with the case of zero altitude, which corresponds to the 2-D FSR [15 (p.441)]. So, in the region close to the receiver the second factor intensifies the first one to provide a higher accuracy in 3-D FSR, whilst the inverse situation takes place in proximity to the transmitter region.

The calculation of rms deviation of the error of estimation of co-ordinate y has shown that it is insignificant in comparison with σ_x and does not have a major effect on the accuracy of target position estimation.

The accuracy of altitude estimation in 3-D FSR has also been evaluated. In Figure 13.32, the dependence of normalised rms deviations of altitude estimation

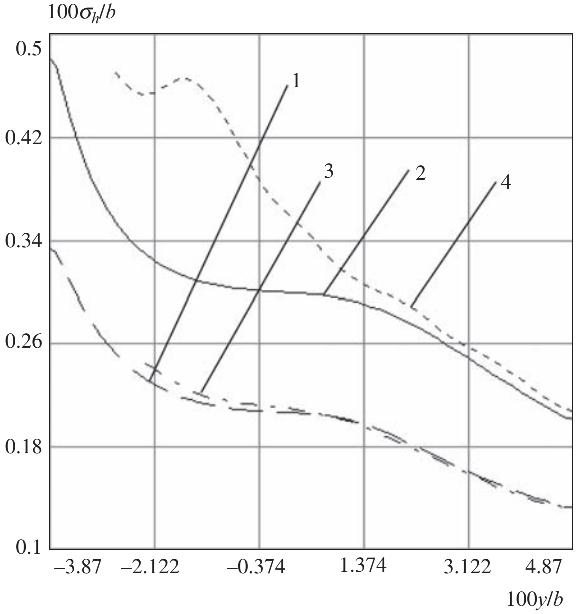

Figure 13.32 Rms deviation of target altitude estimation

errors on the value of co-ordinate y in 3-D FSR is shown. Curve 1 corresponds to the target flight altitude of $h = 1{,}000$ m, curve 2 corresponds to the altitude $h = 2{,}000$ m.

By increasing the altitude, the accuracy of the altitude evaluation falls. This can be easily explained from the viewpoint of geometry – at an equal horizontal range, the linear size of the error region of the altitude estimation increases with the increase of altitude.

13.5.5 Iterative algorithm of co-ordinate estimation

A specific feature of CW FSR is that target co-ordinates cannot be measured directly as well as calculated analytically using measurements of Doppler shift and angles. In practice, iterative algorithms are used in order to obtain the solution of the minimisation problem (13.52), giving the maximal likelihood estimation of the vector of trajectory parameters. The use of the Gauss–Newton algorithm gives [79]:

$$\hat{\mathbf{x}}_n^{i+1} = \hat{\mathbf{x}}_n^{i} + k_C\left(\mathbf{H}_n^T\mathbf{G}_n\mathbf{H}_n\right)^{-1}\mathbf{H}_n^T\mathbf{G}_n\left[\mathbf{z}_n - \mathbf{h}_n(\hat{\mathbf{x}}_n^{i})\right] \tag{13.54}$$

Here, $\hat{\mathbf{x}}_n^{i}$ is the estimate of the vector of trajectory parameters for the ith iteration; $\mathbf{H}_n = \partial\mathbf{h}_n(\mathbf{x})/\partial\mathbf{x}|_{\mathbf{x}=\hat{\mathbf{x}}_n^{i}}$ is the matrix of derivatives; k_C is the parameter determining the rate of convergence.

In a practical application of the given iterative algorithm, the key problem is to choose an initial approximation, $\hat{\mathbf{x}}_n^{0}$ [79,80]. Since the minimised function, $\varphi_n(\mathbf{x}_n)$, is essentially non-linear, the application of the Gauss–Newton algorithm guarantees finding the local minimum, which does not always coincide with the absolute minimum.

Suppose there are two triplets of primary measurements, (f_{D1}, α_1, β_1) and (f_{Dn}, α_n, β_n), taken at the time interval $\Delta t = (n - 1)T$. Using these triplets of primary parameters, a system of six non-linear equations concatenating the values of the primary parameters and the trajectory parameters can be obtained from (13.49). Taking into account that the bistatic angle, β_B, is close to 180°, the proposed system can be presented in a linearised form:

$$\begin{cases} f_{Dn} = -\dfrac{V_y}{\lambda}\left(\alpha_n + \dfrac{y_n}{b - x_n}\right) \\ \alpha_n = \dfrac{y_n}{x_n} \\ \beta_n = \dfrac{z_n}{\sqrt{x_n^2 + y_n^2}} \\ f_{D1} = -\dfrac{V_y}{\lambda}\left(\alpha_1 + \dfrac{y_1}{b - x_1}\right) \\ \alpha_1 = \dfrac{y_1}{x_1} \\ \beta_1 = \dfrac{z_1}{\sqrt{x_1^2 + y_1^2}} \end{cases} \tag{13.55}$$

The obtained system always has a unique solution determined by the expressions [15 (p.423), 79,80]:

$$\begin{cases} x_n = \left(\lambda f_{Dn} f_{D1} \Delta t + b\alpha_1^2 f_{Dn} - b\alpha_n \alpha_1 f_{D1}\right)/u \\ y_n = \alpha_n x_n \\ z_n = \sqrt{{x_n}^2 + {y_n}^2}\,\beta_n \\ V_x = b\left(f_{Dn}\alpha_1^2 + f_{D1}\alpha_n^2 - \alpha_n\alpha_1\left(f_{D1} + f_{Dn}\right)\right)/(u\Delta t) \\ V_y = -\lambda f_{Dn} f_{D1}(\alpha_1 - \alpha_n)/u \end{cases} \tag{13.56}$$

where $u = \lambda f_{Dn} f_{D1} \Delta t/b + f_{Dn}\alpha_1^2 - f_{D1}\alpha_n^2$.

Substitution of the estimates of primary parameters (f_{D1}, α_1, β_1) and (f_{Dn}, α_n, β_n) into (13.56) allows the finding of an initial approximation for the trajectory parameters vector, $\hat{\mathbf{x}}_n^0$. Better results can be achieved if an initial approximation is found using all primary measurements obtained [15 (p.423), 79,80]. Using the least squares method, from the available samples, we can obtain a polynomial approximation of the Doppler shift, f_D, azimuth, α and elevation angle, β. A polynomial of arbitrary degree can be used, but usually it is a linear approximation which yields:

$$\begin{aligned} \tilde{f}_D(t) &= a_f t + b_f \\ \tilde{\alpha}(t) &= a_\alpha t + b_\alpha \\ \tilde{\beta}(t) &= a_\beta t + b_\beta \end{aligned} \tag{13.57}$$

where:

$$\begin{aligned} a_{f(\alpha,\beta)} &= \frac{\sum\limits_{i=1}^{N}(t_i - \hat{m}_t)(\hat{f}_i - \hat{m}_{f(\alpha,\beta)})}{\sum\limits_{i=1}^{N}(t_i - \hat{m}_t)^2} \\ b_{f(\alpha,\beta)} &= \hat{m}_{f(\alpha,\beta)} - a_{f(\alpha,\beta)}\hat{m}_t \end{aligned} \tag{13.58}$$

Substituting f_{D1}, α_1, β_1, f_{Dn}, α_n, β_n in (13.56) for estimates $\tilde{f}_{D1}$, $\tilde{\alpha}_1$, $\tilde{\beta}_1$, $\tilde{f}_{DN}$, $\tilde{\alpha}_N$, $\tilde{\beta}_N$, we obtain the sought after initial approximation.

Using the iterative algorithm (13.54) and initial approximation (13.56), the estimations of the target co-ordinate measurement accuracy were obtained by the mathematical modelling. The statistics of primary measurement errors were accepted as being Gaussian and averaging was made on 1,000 independent realisations. System parameters and trajectories were similar to those that have been described in the calculation of potential accuracy. In Figures 13.31 and 13.32,

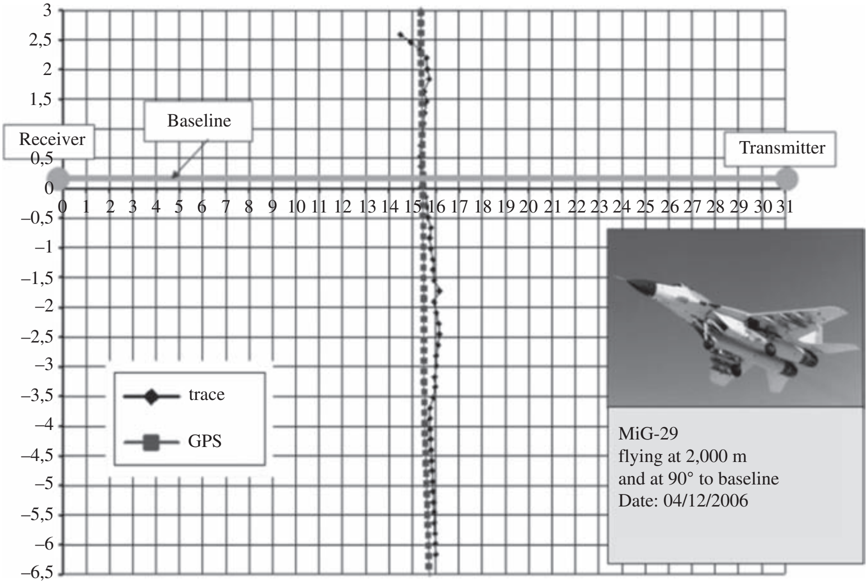

MiG-29
flying at 2,000 m
and at 90° to baseline
Date: 04/12/2006

Figure 13.33 Results of tracking of fighter MIG-29

dotted and dash-dotted lines present the results of the modelling. Curves labelled 3 correspond to the target altitude of 1,000 m, curves labelled 4 correspond to an altitude of 2,000 m. It is seen from the comparison of the theoretical curves and curves obtained during modelling, that the described iterative algorithm provides close to maximum potential target tracking accuracy. Parametric ambiguity with respect to the correlation matrix of errors of primary measurements can be eliminated during tracking.

13.5.6 Experimental tracking results

Experiments with the tracking of air targets were carried out on a full-scale basis. In experimental FSR, air target trajectories were estimated using the iterative algorithm considered earlier, on the basis of the maximum likelihood method. A first approximation of the trajectory parameter vector was obtained from the first six primary measurements. The primary measurement interval T was set to be 1 s. The Doppler frequency shift and azimuth measurement variances were estimated during target tracking. The true trajectories were obtained using the data provided by the onboard GPS equipment.

Figures 13.33 and 13.34 show the results of a target-tracking experiment. Thus, the experiment validated the suitability of the maximum likelihood algorithm for establishing trajectory parameters with sufficient accuracy in real time.

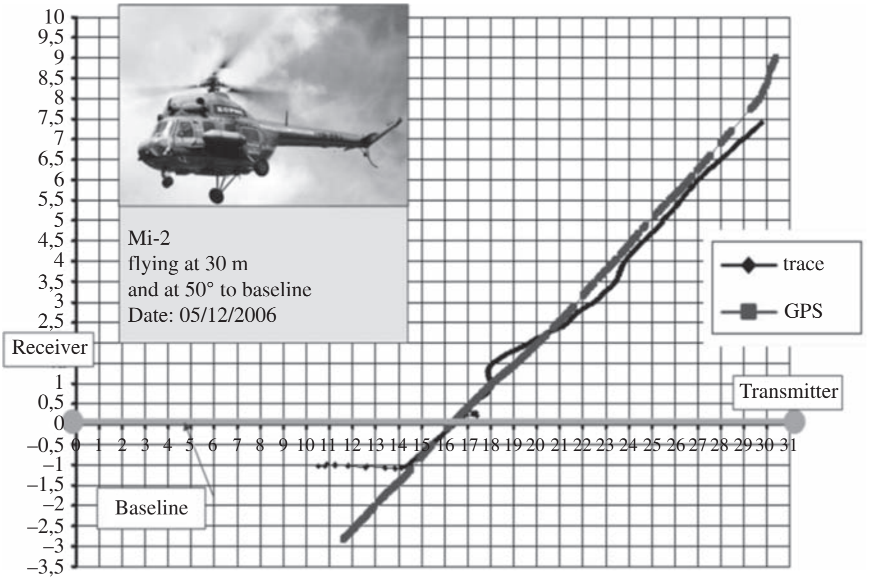

Figure 13.34 Results of tracking of helicopter Mi-2

List of abbreviations

BPF	band pass filter
CW	continuous wave
DPS	direct path signal
EM	electromagnetic
FS	forward scatter
FSCS	forward scatter cross-section
FSR	forward scatter radar
HPF	high pass filter
LPF	low pass filter
LS	leakage signal
PDF	probability density function
PO	physical optics
PSD	power spectrum (spectral) density
PTD	physical theory of diffraction
RCS	radar cross-section
RSSI	received signal strength indicator
Rx	receive/receiver

SLD	square law detector
SNR	signal-to-noise ratio
SS	sea state
TRP	two ray path
Tx	transmit/transmitter
UAV	unmanned aerial vehicle
UHF	Ultra-high frequency
VHF	Very high frequency

References

[1] Willis, N.J.: *Bistatic Radar* (Raleigh, SciTech Publishing, Inc., 2005, 2nd edn.).

[2] Naka, F.R., Ward, W.W.: ‘Distant Early Warning Line Radars: The Quest for Automatic Signal Detection’ *Lincoln Lab. J.*, 2000, 12, (2), pp. 181–204.

[3] Glaser, J.: ‘Forward Scatter Radar for Future Systems’ *WSTIAC Q.*, 2011, 10, (3), pp. 3–8.

[4] Cherniakov, M., Gashinova, M., Cheng, H., Antoniou, M., Sizov, V., Daniel, L.Y.: ‘Ultra Wideband Forward Scattering Radar: Concept and Prospective’, ‘Radar Syst. 2007 IET Int. Conf.’, (2007), pp. 1–5.

[5] Daniel, L.Y., Hoare, E.G., Gashinova, M., Svintsov, A., Cherniakov, M., Sizov, V.: ‘Ultra-Wideband Forward Scatter Radar Fence for Maritime Surveillance – Initial Experimental Results’, in ‘Radar Conf. 2010 IEEE’ (2010), pp. 526–531.

[6] Cherniakov, M., Abdullah, R.S.A.R., Jancovic, P., Salous, M., Chapursky, V.: ‘Automatic Ground Target Classification using Forward Scattering Radar’ *IEE Proc. Radar, Sonar Navig.*, 2006, 153, (5), pp. 427–437.

[7] Chapurskiy, V.V., Sablin, V.N.: ‘SISAR: Shadow Inverse Synthetic Aperture Radiolocation’, in ‘Record of the IEEE 2000 International Radar Conference’ (IEEE, 2000), pp. 322–328.

[8] Gashinova, M., Daniel, L., Hoare, E., Kabakchiev, K., Cherniakov, M., Sizov, V.: ‘Forward Scatter Radar Mode for Passive Coherent Location Systems’, in IEEE Int. Radar Conf. 2013, (1), pp. 235–239.

[9] Sizov, V., Gashinova, M., Zakaria, N., Cherniakov, M.: ‘VHF Communication Channel Characterisations Over Complex Wooded Propagation Paths with Applications to Ground Wireless Sensor Networks’ *IET Microw., Antennas Propag.*, 2013, 7, (3), pp. 166–174.

[10] Zeng, T., Hu, C., Cherniakov, M., Zhuo, C., Mao, C.: ‘Joint Parameter Estimation and Cramer-Rao Bound Analysis in Ground-based Forward Scatter Radar’ *EURASIP J. Adv. Signal Process.*, 2012, (1), p. 80.

[11] Gashinova, M., Daniel, L., Hoare, E., Sizov, V., Kabakchiev, K., Cherniakov, M.: ‘Signal Characterisation and Processing in the Forward

Scatter Mode of Bistatic Passive Coherent Location Systems' *EURASIP J. Adv. Signal Process.*, 2013, (1), p. 1.

[12] Hristov, S., Daniel, L., Hoare, E., Cherniakov, M., Gashinova, M.: 'Target Shadow Profile Reconstruction in Ground-based Forward Scatter Radar', in 2015 IEEE Radar Conference, pp. 0846–0851.

[13] Ufimtsev, P.Y.: *Fundamentals of the Physical Theory of Diffraction* (Hoboken, John Wiley & Sons, Inc., 2007, 1st edn.).

[14] Pathak, P.H.: 'Techniques for High-Frequency Problems', in Lo, Y.T., Lee, S.W. (Eds.): *Antenna Handbook: Theory, Applications and Design* (New York, Springer Science+Business Media, 1988, 1st edn.), pp. 195–311.

[15] Cherniakov, M.: *Bistatic Radars: Principles and Practice* (Chichester, John Wiley & Sons Ltd, 2007, 1st edn.).

[16] Ufimtsev, P.Y.: 'New Insight into the Classical Macdonald Physical Optics Approximation' *IEEE Antennas Propag. Mag.*, 2008, 50, (3), pp. 11–20.

[17] Gashinova, M., Kabakchiev, K., Daniel, L., Hoare, E., Sizov, V., Cherniakov, M.: 'Measured Forward-scatter Sea Clutter at Near-zero Grazing Angle: Analysis of Spectral and Statistical Properties' *IET Radar, Sonar Navig.*, 2014, 8, (2), pp. 132–141.

[18] Hu, C., Sizov, V., Antoniou, M., Gashinova, M., Cherniakov, M.: 'Optimal Signal Processing in Ground-Based Forward Scatter Micro Radars' *IEEE Trans. Aerosp. Electron. Syst.*, 2012, 48, (4), pp. 3006–3026.

[19] Chernyak, V.S.: *Fundamentals of Multisite Radar Systems* (Amsterdam, Gordon and Breach Science Publishers, 1998, 1st edn.).

[20] Gashinova, M., Daniel, L., Kabakchiev, K., Sizov, V., Hoare, E., Cherniakov, M.: 'Phenomenology of Signals in FSR for Surface Targets Detection' *Radar Syst.*, *IET Int. Conf.*, 2012, pp. 1–6. *(Radar 2012).*

[21] Mie, G.: 'Beiträge zur Optik trüber Medien, speziell kolloidaler Metallösungen' *Ann. Phys.*, 1908, 330, (3), pp. 377–445.

[22] Balanis, C.A.: *Antenna Theory – Analysis and Design* (New York, John Wiley & Sons, Inc., 1997, 2nd edn.).

[23] Hristov, S., Daniel, L., Hoare, E., Cherniakov, M., Gashinova, M.: 'Target Shadow Profile Reconstruction in Ground-based Forward Scatter Radar', in '2015 IEEE Radar Conference (RadarCon)' (IEEE, 2015), pp. 0846–0851.

[24] 'CST Microwave Studio', https://www.cst.com/Products/CSTMWS. Last accessed on 14 July 2017.

[25] Gashinova, M., Daniel, L., Sizov, V., Hoare, E., Cherniakov, M.: 'Phenomenology of Doppler Forward Scatter Radar for Surface Targets Observation' *IET Radar, Sonar Navig.*, 2013, 7, (4), pp. 422–432.

[26] Daniel, L., Gashinova, M., Cherniakov, M.: 'Maritime Target Cross Section Estimation for an Ultra-wideband Forward Scatter Radar Network', in '2008 Eur. Radar Conf.' (2008), (October), pp. 316–319.

[27] Sizov, V., Cherniakov, M., Antoniou, M.: 'Forward Scattering Radar Power Budget Analysis for Ground Targets' *IET Radar, Sonar Navig.*, 2007, 1, (6), p. 437.

[28] Long, T., Hu, C., Cherniakov, M.: ‘Ground Moving Target Signal Model and Power Calculation in Forward Scattering Micro Radar’ *Sci. China Ser. F, Inf. Sci.*, 2009, 52, (9), p. 11.

[29] Sizov, V., Gashinova, M., Rashid, N.E., Chen, J., Cherniakov, M.: ‘Forward Scattering Micro Radar Efficiency Analysis for Different Landscapes’, in *‘6th EMRS DTC Tech. Conf.’* (2009), (1), p. 7.

[30] Nathanson, F.E.: *Radar Design Principles* (Mendham, SciTech Publishing, Inc., 1999, 2nd edn.).

[31] Parsons, J.D.: *The Mobile Radio Propagation Channel* (Chichester, John Wiley & Sons Ltd, 2000, 2nd edn.).

[32] Skolnik, M.J.: *Introduction to Radar Systems* (New York, McGraw-Hill, 2001, 3rd edn.).

[33] Kerr, D.E.: *Propagation of Short Radio Waves* (New York, Dover Publications, Inc., 1965, 1st edn.).

[34] Sizov, V., Cherniakov, M., Antoniou, M.: ‘Forward Scattering Radar Power Budget Analysis for Ground Targets’ *IET Radar, Sonar Navig.*, 2007, 1, (6), p. 437.

[35] Ament, W.S.: ‘Toward a Theory of Reflection by a Rough Surface’ *Proc. IRE*, 1953, 41, (1), pp. 142–146.

[36] Rappaport, T.S.: *Wireless Communications: Principles and Practice* (Upper Saddle River, Prentice Hall PTR, 2001, 2nd edn.).

[37] Briggs, J.: *Target Detection by Marine Radar* (London, The Institution of Electrical Engineers, 2004, 1st edn.).

[38] Cherniakov, M., Salous, M., Kostylev, V., Abdullah, R.: ‘Analysis of Forward Scattering Radar for Ground Target Detection’, in ‘EURAD 2005 Conf. Proc. – 2nd Eur. Radar Conf., 2005’ (2005), pp. 165–168.

[39] Kabakchiev, K., Daniel, L.Y., Sizov, V., Hoare, E.G., Gashinova, M., Cherniakov, M.: ‘Received Signal Characterization in Forward Scatter Radar for Maritime Application’, in ‘Radar Symposium (IRS), 2011 Proceedings International’ (2011), pp. 67–72.

[40] Antoniou, M., Sizov, V., Hu, C., *et al.*: ‘The Concept of a Forward Scattering Micro-Sensors Radar Network for Situational Awareness’, ‘Proc. 2008 Int. Conf. Radar, Radar 2008’ (2008), pp. 171–176.

[41] Hu, C., Sizov, V., Antoniou, M., Gashinova, M., Cherniakov, M.: ‘Optimal Signal Processing in Ground-Based Forward Scatter Micro Radars’ *IEEE Trans. Aerosp. Electron. Syst.*, 2012, 48, (4), pp. 3006–3026.

[42] Hiatt, R., Siegel, K., Weil, H.: ‘Forward Scattering by Coated Objects Illuminated by Short Wavelength Radar’ *Proc. IRE*, 1960, 48, (9), pp. 1630–1635.

[43] Levanon, N., Mozeson, E.: *Radar Signals* (Hoboken, John Wiley & Sons, Inc., 2004, 1st edn.).

[44] Ufimtsev, P.Y.: ‘The 50-Year Anniversary of the PTD: Comments on the PTD’s Origin and Development’ *IEEE Antennas Propag. Mag.*, 2013, 55, (3), pp. 18–28.

[45] Ruck, G.T., Barrick, D.E., Stuart, K.M., Kirchbaum, C.K.: *Radar Cross Section Handbook: Volume 1* (New York, Plenum Press, 1970, 1st edn.).

[46] Ross, R.A.: ‘Forward Scattering from A Finite, Circular Cylinder’ *Prog. Electromagn. Res. C*, 2008, 2, pp. 207–215.

[47] Glaser, J.: ‘Bistatic RCS of Complex Objects near Forward Scatter’ *IEEE Trans. Aerosp. Electron. Syst.*, 1985, AES-21, (1), pp. 70–78.

[48] Marra, M., De Luca, A., Hristov, S., Daniel, L., Gashinova, M., Cherniakov, M.: ‘New Algorithm for Signal Detection in Passive FSR’, in ‘2015 IEEE Radar Conference’, pp. 218–223.

[49] Abdullah, R., Cherniakov, M., Janovic, P., Salous, M.: ‘Progress on Using Principle Component Analysis in FSR for Vehicle Classification’, in ‘2nd International Workshop On Intelligent Transportation’ (2005), pp. 7–12.

[50] Myakinkov, A., Kuzin, A., Gashinova, M., Sizov, V., Cherniakov, M.: ‘Inverse Forward Scatter SAR’, in ‘Proceedings of International Conference on Synthetic Aperture Sonar and Synthetic Aperture Radar’ (2010), pp. 152–156.

[51] Van Trees, H.L., Bell, K.L., Tian, Z.: *Detection Estimation and Modulation Theory – Part 1: Detection, Estimation, and Filtering Theory* (Hoboken, John Wiley & Sons, Inc., 2013, 2nd edn.).

[52] Billingsley, J.B.: *Low-angle Radar Land Clutter: Measurements and Empirical Models* (Norwich, William Andrew Publishing/Noyes Publishing, 2002, 1st edn.).

[53] Sizov, V., Gashinova, M., Zakaria, N., Cherniakov, M.: ‘VHF Communication Channel Characterisations Over Complex Wooded Propagation Paths with Applications to Ground Wireless Sensor Networks’ *IET Microwaves, Antennas Propag.*, 2013, 7, (3), pp. 166–174.

[54] Joshi, G.G., Dietrich, C.B., Anderson, C.R., *et al.*: ‘Near-ground Channel Measurements Over Line-of-Sight and Forested Paths’ *IEE Proc. – Microw., Antennas Propag.*, 2005, 152, (6), p. 589.

[55] Cheffena, M., Ekman, T.: ‘Dynamic Model of Signal Fading due to Swaying Vegetation’ *EURASIP J. Wirel. Commun. Netw.* 2009, 2009, pp. 1–11.

[56] Cheffena, M., Ekman, T.: ‘Modeling the Dynamic Effects of Vegetation on Radiowave Propagation’, in ‘2008 IEEE International Conference on Communications’ (IEEE, 2008), pp. 4466–4471.

[57] Gashinova, M., Cherniakov, M., Zakaria, N.A., Sizov, V.: ‘Empirical Model of Vegetation Clutter in Forward Scatter Radar Micro-sensors’, in ‘2010 IEEE Radar Conference’, pp. 899–904.

[58] Daniel, L., Gashinova, M., Cherniakov, M.: ‘Maritime UWB Forward Scattering Radar Network: Initial Study’, in ‘2008 International Conference on Radar’ (IEEE, 2008), pp. 658–663.

[59] Kabakchiev, K., Daniel, L., Gashinova, M., Hoare, E., Cherniakov, M., Sizov, V.: ‘Radar Parameters Influence on the Clutter in Maritime Forward Scatter Radar’, in ‘2014 11th European Radar Conference’ (IEEE, 2014), pp. 113–116.

[60] De Luca, A., Daniel, L., Kabakchiev, K., Hoare, E., Gashinova, M., Cherniakov, M.: ‘Maritime FSR with Moving Receiver for Small Target Detection’, in ‘2015 16th International Radar Symposium (IRS)’ (IEEE, 2015), pp. 834–839.

[61] Berry, R.: ‘Radar Propagation at Very Low Altitude over the Sea’, in ‘Radar-present and Future’ (1973), pp. 140–145.

[62] Williams, P.D.L., Cramp, H.D., Curtis, K.: ‘Experimental Study of the Radar Cross-section of Maritime Targets’ *IEE J. Electron. Circuits Syst.*, 1978, 2, (4), p. 121.

[63] Fabbro, V., Bourlier, C., Combes, P.F.: ‘Forward Propagation Modeling Above Gaussian Rough Surfaces by the Parabolic Shadowing Effect’ *Prog. Electromagn. Res.*, 2006, 58, pp. 243–269.

[64] Zujkov, V.A., Pedenko, Y.A., Razskazovsky, V.B.: ‘Characteristics of Radio Propagation in Sea Surface Layer, Propagation of Radio Waves of Millimeter and Centimeter Bands’, in ‘Proc. of IRE AN USSR’ (1989), pp. 76–82.

[65] Pedenko, Y.A., Razskazovsky, V.B.: ‘Multipath Propagation over Sea, Radiophysical Study of the World Ocean’, in *‘Proc. of IRE AN USSR’* (1992), pp. 32–50.

[66] Beard, C., Katz, I., Spetner, L.: ‘Phenomenological Vector Model of Microwave Reflection from the Ocean’ *IRE Trans. Antennas Propag.*, 1956, 4, (2), pp. 162–167.

[67] Beard, C., Katz, I.: ‘The Dependence of Microwave Radio Signal Spectra on Ocean Roughness and Wave Spectra’ *IRE Trans. Antennas Propag.*, 1957, 5, (2), pp. 183–191.

[68] Smith, J.R., Russell, S.J., Brown, B.E., *et al.*: ‘Electromagnetic Forward-Scattering Measurements Over a Known, Controlled Sea Surface at Grazing’ *IEEE Trans. Geosci. Remote Sens.*, 2004, 42, (6), pp. 1197–1207.

[69] Freund, D.E., Woods, N.E., Ku, H.-C., Awadallah, R.S.: ‘Forward Radar Propagation Over a Rough Sea Surface: A Numerical Assessment of the Miller-Brown Approximation Using a Horizontally Polarized 3-GHz Line Source’ *IEEE Trans. Antennas Propag.*, 2006, 54, (4), pp. 1292–1304.

[70] Hristov, T.S., Anderson, K.D., Friehe, C.A.: ‘Scattering Properties of the Ocean Surface: The Miller–Brown–Vegh Model Revisited’ *IEEE Trans. Antennas Propag.*, 2008, 56, (4), pp. 1103–1109.

[71] Brown, R.M., Miller, A.R.: ‘Geometric-Optics Theory for Coherent Scattering of Microwaves from the Ocean Surface’, 1974, Technical Report, Naval Research Laboratory, Washington, D.C.

[72] Miller, A.R., Brown, R.M., Vegh, E.: ‘New Derivation for the Rough-Surface Reflection Coefficient and for the Distribution of Sea-Wave Elevations’ *IEE Proc. H Microwaves, Opt. Antennas*, 1984, 131, (2), pp. 114–116.

[73] Beard, C.I.: ‘Coherent and Incoherent Scattering of Microwaves from the Ocean’ *IRE Trans. Antennas Propag.*, 1961, 9, (5), pp. 470–483.

[74] Anderson, K., Doss-Hammel, S., Tsintikidis, D., *et al.*: ‘The RED Experiment: An Assessment of Boundary Layer Effects in a Trade Winds Regime on Microwave and Infrared Propagation over the Sea’ *Bull. Am. Meteorol. Soc.*, 2004, 85, (9), pp. 1355–1365.

[75] Blyakhman, A.B., Runova, I.A.: 'Forward Scattering Radiolocation Bistatic RCS and Target Detection', in 'Proceedings of the 1999 IEEE Radar Conference. Radar into the Next Millennium' (IEEE, 1999), pp. 203–208.

[76] Ryndyk, A.G., Kuzin, A.A., Myakinkov, A.V., Blyakhman, A.: 'Target Tracking in Forward Scattering Radar with Multi-beam Transmitting Antenna', in 'International Radar Conference – Surveillance for a Safer World, 2009. RADAR 2009.' pp. 1–4.

[77] Blyakhman, A.B., Ryndyk, A.G., Myakinkov, A.V., Burov, V.N.: 'Algorithm of Trajectory Tracking the Targets, which are Moving along the Curvilinear Trajectories in the Bistatic Forward-scattering Radar System', in 'IET International Conference on Radar Systems (Radar 2012)' (Institution of Engineering and Technology, 2012), pp. 1–4.

[78] Blyakhman, A.B., Myakinkov, A.V., Ryndyk, A.G.: 'Tracking Algorithm for Three-Dimensional Bistatic Forward Scattering Radar with Weighting of Primary Measurements', in 'European Radar Conference, EURAD 2005.' (IEEE, 2005), pp. 153–156.

[79] Blyakhman, A.B., Ryndyk, A.G., Sidorov, S.B.: 'Forward Scattering Radar Moving Object Coordinate Measurement', in 'Record of the IEEE 2000 International Radar Conference' (IEEE, 2000), pp. 678–682.

[80] Blyakhman, A.B., Myakinkov, A.V., Ryndyk, A.G.: 'Algorithm of Target Tracking for Three-Dimensional Bistatic Forward Scattering Radar', in 'Proc. IV International Radar Symposium' (2004), pp. 309–324.

[81] Myakinkov, A.V., Ryndyk, A.G.: 'Space-time Processing in Three-Dimensional Forward Scattering Radar', in '4th International Conference on Antenna Theory and Techniques' (IEEE, 2003), pp. 355–358.

[82] Myakinkov, A.V.: 'Optimal Detection of High-Velocity Targets in Forward Scattering Radar', in '5th International Conference on Antenna Theory and Techniques, 2005.' (IEEE, 2005), pp. 345–347.

[83] Sage, A.P., Melsa, J.L.: *Estimation Theory with Applications to Communications and Control* (New York, McGraw-Hill, 1971, 1st edn.).